Pineda, N., O. Rodríguez, A. del Moral Méndez, J. Montanyà, O. van der Velde, and S. Castán, 2026: Total lightning for early warning: The Iberian tornadic supercell with giant hail on 6 July 2023. *Electronic J. Severe Storms Meteor.,* **21** (2), 1–36.

Electronic Journal of
SEVERE STORMS METEOROLOGY

Total Lightning for Early Warning: The Iberian Tornadic Supercell with Giant Hail on 6 July 2023

NICOLAU PINEDA, ORIOL RODRÍGUEZ
Meteorological Service of Catalonia, Barcelona, Spain

ANNA DEL MORAL MÉNDEZ
Earth Observing Laboratory, NSF National Center for Atmospheric Research, Boulder, CO

JOAN MONTANYÀ, OSCAR VAN DER VELDE
Technical University of Catalonia, Terrassa, Spain

SALVADOR CASTÁN
Agencia Pericial, Cornellà de Llobregat, Spain

(Submitted 5 May 2025; in final form 30 August 2026)

ABSTRACT

On 6 July 2023, a severe-thunderstorm outbreak took place in the northeastern Iberian Peninsula. The analysis targets the Mid Ebro Valley, south of the city of Zaragoza, where giant hail was recorded (diameter ø >10 cm) along with damaging winds (i.e., an IF1.5 tornado and three IF2 nontornadic events). We specifically analyze severe-weather patterns observable in radar and satellite products, with particular emphasis on total-lightning signatures from the real-time data provided by the lightning mapping array (LMA) in the region. Prior to the severe weather reported on the ground, a persistent "lightning-hole" signature was identified in the LMA data. This feature was collocated with the bounded weak echo region (BWER) radar signature. Additionally, high-altitude LMA sources, referred to as overshooting lightning or "sparkles", were detected within the storm's overshooting tops (at 15–16 km MSL). These discharges, suspended 1–2 km above the primary lightning activity, indicate deep, moist convection. These severe-weather signatures complement the lightning "jump" as early warning indicators for forecasters. This case study helps us to demonstrate the advantages of integrating LMA real-time data along with radar and satellite products for severe-weather surveillance. Total-lightning information provides forecasters with additional tools for identifying areas where convection is forming or intensifying, enhancing their confidence in the decision-making process and prompting warnings of potential severe weather.

1. Introduction

Accurate data are needed to create decision-support tools, especially as meteorological services emphasize the importance of improving severe-weather forecasts and alerts (e.g., Blair et al. 2017). Future forecasters shall be skilled in nowcasting and warning operations, employing both established and emerging technologies to predict the effects of hazards more accurately, such as damaging hailstorms and tornadoes (e.g., Craven et al. 2015).

Radar-based products, using both equivalent reflectivity factor (hereafter referred to as reflectivity factor), radial velocity and, more recently, polarimetric moments, have been the principal tools for weather surveillance over the past several decades (e.g., Donavon and Jungbluth 2007; Blair et al. 2011; Kumjian and Ryzhkov 2008).

Corresponding author address:
Nicolau Pineda, Barcelona, Spain,
E-mail: nicolau.pineda@gencat.cat

Typical reflectivity radar signatures, like the BWER, a weak radar reflectivity region signaling strong updrafts (Lemon 1980), or the three-body scatter spike (TBSS), a signature related to the presence of large hail (e.g., Zrnić et al. 2010; Lindley and Lemon 2007), have been widely used to forecast severe weather in the short term.

Research has shown that the integration of total-lightning data with radar products enhances forecasters' capabilities in short-term convective weather forecasting (e.g., Darden et al. 2010; Stano et al. 2014). Total-lightning density portrays structural information complementary to that observed with radars. Total lightning retrieved from lightning mapping array (LMA) networks can depict the structure of a thunderstorm in a way similar to how radar observations show typical storm features (Chmielewski et al. 2018).

Most supercells are prolific producers of lightning, and different works (e.g., Goodman et al. 2005; Steiger et al. 2007) indicate they may possess distinctive lightning characteristics. For instance, a “lightning hole” is a void of electrical activity coincident with the strong, rotating updraft (Emersic et al. 2011; Calhoun et al. 2013). Furthermore, lightning bursts observed in the overshooting top indicate deep convection (e.g., Krehbiel et al. 2000; Lyons et al. 2003).

All in all, total-lightning signatures are a significant research topic because of their relevance in connecting electrical, kinematic, and microphysical processes in severe storms. In addition to the lightning jump, which is a well-known signal for warning about impending severe weather (e.g., Schultz et al. 2011; Metzger and Nuss 2013; Farnell et al. 2017), distinctive lightning characteristics such as the lightning hole, as well as overshooting lightning, also help in forecasting severe weather.

This research aims to demonstrate, via a case study, the advantages of integrating total lightning with radar and satellite data for warning-decision support during severe-weather surveillance. We specifically analyze the tornadic supercell from 6 July 2023, which was associated with reports of giant hail. Although total-lightning signatures are less familiar to forecasters, they complement those observed by radar, enhancing their confidence in the decision-making process and triggering warnings of possible severe weather on the ground. We do not aim to deliver a comprehensive analysis of the case study, but rather to focus on identifying severe-weather signatures that can be observed in radar, satellite and total lightning throughout the supercell evolution.

Section 2 presents the data and method. Section 3 describes the severe-weather outbreak on July 6, 2023, and the synoptic framework. Section 4 examines severe-weather patterns. Section 5 facilitates the discussion, while Section 6 presents the conclusions. Finally, appendices include: a) the results of the damage assessment from strong convective winds done onsite after the severe-weather event, b) the estimated effectiveness of the LMA network, and c) relevant photos that confirm the presence of severe weather.

2. Data and methodology

a. Region of study

The Ebro basin is one of the major topographic depressions in the Iberian Peninsula (southwestern Europe). Various mountain ranges surround the valley, with the Cantabrian Range and the Pyrenees to the north, the Iberian Mountains to the west, and the Coastal Mediterranean Range to the east (Fig. 1).

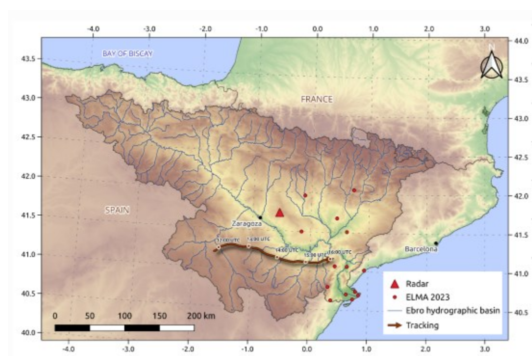

Figure 1: Supercell trajectory across the Middle Ebro Valley (black arrow) within the Ebro River catchment (grey contour). Storm’s life cycle was in the coverage area of the Spanish meteorological agency (AEMET)’s Zaragoza radar (N 41.734039°, E –0.545893°) (red triangle), as well as on the domain of the Ebro Lightning Mapping Array (ELMA stations as red points). *Click image to enlarge.*

The area of interest is the Middle Ebro Valley, a corridor facilitating the entrance of contrasted air masses from the northwest (typically cool and arid) and the southeast (warm and humid). The central area of the Middle Ebro Valley experiences the highest supercell density of the Iberian Peninsula (Martín et al. 2020). The literature has long discussed this area as one of the European continent's regions most prone to severe-weather activity (Punge and Kunz 2016). García-Ortega et al. (2011) pointed to the Ebro Valley as having the highest frequency of hailstorms in the entire Iberian Peninsula, with a yearly average of ≈30 hailstorm days between May and September.

b. Lightning mapping array

The Ebro Lightning Mapping Array (ELMA) network consists of 12 LMA stations deployed across the low Ebro River valley and delta (Fig. 1). The LMA system locates the sources of impulsive very high frequency (VHF) radio signals (60–66 MHz) from lightning channels by precisely timing the signals' arrival at each receiving station, with a temporal resolution of 80 μs at a time (Rison et al. 1999). This frequency range allows for the detection of smaller-scale breakdown processes such as branching and leader development, allowing for the 3D mapping of lightning. Time-of-arrival techniques process the data, revealing the horizontal, vertical and temporal location of each VHF source, with location errors ranging from tens of meters within the network limits. Since each station records the peak received power of each event, the processed data also includes an estimation of the total peak power radiated by the sources (Thomas et al. 2001).

Ultimately, the goodness of fit is determined by the reduced χ^2 value (Thomas et al. 2004). To be considered in this analysis, an LMA source needed to have a maximum reduced χ^2 value of 1.0. The detection efficiency of LMA networks within the network range is typically greater than 95%, although it decreases quickly outside of 150 km of the network center (Koshak et al. 2004; Chmielewski and Bruning 2016). Whereas the initial stage was on the edge of the network coverage, the storm progressed to the center of the network (see trajectory in Fig. 1).

Reconstructing up to hundreds of sources per flash allows for accurate three-dimensional lightning image maps. Because of the high rate of emissions detected per lightning flash in the VHF frequency (with multiple emissions per lightning channel), these data enable the "mapping" of the full spatial extent of lightning propagation. Calculation of flash sizes and rates requires that the VHF sources be grouped into flashes. The lightning algorithm relies on the temporal and spatial proximity of consecutive sources, classifying them as either part of a flash or noise (McCaul et al. 2005, 2009). Specifically, we used the algorithm by van der Velde and Montanyà (2013). Firstly, the algorithm filters out sources that appear unrelated to lightning activity by considering a specific number of VHF sources (n = 3) within a grid box (x = 3 km, y = 3 km, z = 0.8 km). Then, the algorithm performs the grouping using a designated temporal interval between each successive source (n = 0.15 s). In the final step, we apply a minimum-source filter (n = 10) to validate only lightning that has enough sources to provide evidence for leader propagation, as well as to make results comparable to previous studies that used the same minimum-source filter (e.g., Schultz et al. 2009, 2017, and Chronis et al. 2015).

We used the tool developed by van der Velde (2024) to visualize and analyze LMA data. We calculated lightning "jumps" using the Gatlin and Goodman (2010) algorithm, sampling the total flash rate every 2 min. The mean and standard deviation of the flash-rate change were computed from the previous 10 samples (i.e., a 20-min moving history).

c. Weather radar

We used measurements from the Zaragoza radar (N 41.734°, E –0.546°), operated by AEMET, the Spanish meteorological agency, to complement lightning observations. AEMET operates a network of fifteen C-band (5.4 cm wavelength) Doppler single-polarization radars (WSR-74) covering Spain (Martín et al. 2020). Each of these radars operates with an unambiguous range of 240 km with a 10-min cycle, producing polar volumes with twenty-one elevations. With a single-polarization radar, our case study is constrained to the analysis of the reflectivity factor [Z, dBZ] and radial velocity [V, m s^{-1}] radar moments. However, the analysis of the radial velocity field reveals missing data bins in various sweeps, especially in high azimuthal-shear regions. This anomaly could be the result of aggressive automated filter processing applied in the operational chain. For this reason, the analysis presented here will be focused on *Z* and derived products: ZMAX, TOP, VIL and pseudo-RHI.

ZMAX, in dB*Z*, is the maximum *Z* for each pixel coordinate. The echo-top height (TOP, in dB*Z*) estimates the maximum height at which the radar detects an echo above a specific threshold (e.g., TOP-15, TOP-35, TOP-50, in dB*Z*). Vertically integrated liquid (VIL) is a radar-derived parameter that estimates the total liquid-water content within a storm column by vertically integrating reflectivity values, and is commonly used as an indicator of precipitation intensity and hail potential. Finally, pseudo-RHIs are range-height indicator displays, simulating a vertical cross-section at a given azimuth, retrieved from sweeps in the radar volume.

The ZMAX and pseudo-RHI products were derived after mapping the radar data from polar coordinates into a three-dimensional Cartesian grid, with a 500-m horizontal and vertical resolution, and extending up to 18 km MSL. For the pseudo-RHI, the azimuth of each gridded column was computed, and the desired one was then selected within a 1° confidence interval (i.e., the width of the RHI slice).

d. METEOSAT

Although the analysis mainly relies on radar and lightning data, images from the Meteosat Second Generation (MSG) satellite are sometimes used to look for signs of severe weather, like the storm's overshooting tops and its V shape, as well as the above-anvil cirrus plume. Strong updrafts in deep convection create overshooting tops, which are cloud tops that rise above the normal level in the tropopause and extend into the lower stratosphere (e.g., Bedka 2011). The MSG “sandwich” product (Setvák et al. 2012) is used to analyze this cloud top morphology. This product combines cloud-top brightness temperatures from the 10.8-μm channel, along with the cloud-top shadows and textures that can be seen in the high-resolution visible channel.

e. ERA5 reanalysis

We analyzed the synoptic framework and assessed the preconvective thermodynamic and kinematic conditions using data from ERA5, the latest global ECMWF reanalysis (Hersbach et al. 2020). ERA5 offers hourly data at a resolution of 0.25° for 137 σ or 37 pressure levels. We retrieved the temperature at 850 and 500 hPa, the geopotential height at 500 hPa, the horizontal wind components at 300 hPa, and the dewpoint at 2 m for the synoptic scale analysis. Moreover, to assess the preconvective and convective environments, vertical profiles of temperature, dewpoint, and wind were retrieved using σ-levels data from the closest grid point to the thunderstorm formation location and to the giant hail reports through the ThundeR package (ThundeR 2024).

To examine deep, moist convection and severe-weather environments, we calculated several parameters commonly used in weather surveillance and forecasts, including lapse rate (LR) for several layers, the most-unstable CAPE, lifting condensation level (LCL), equilibrium level (EL), deep-layer shear (0–6 km, DLS), and mid-level shear (0–3 km MLS). We computed these using the ThundeR package. Moreover, we also calculated the convective cloud depth (the difference between EL and LCL, CCD, Taszarek et al. 2020) and the square root of the product of twice the most-unstable CAPE and the MLS (WMAXSHEAR03, Rodríguez and Bech 2021). We used the most-unstable parcel in order to evaluate the initiation of convection from any level, not only from the near-surface layer. The altitude of significant isotherms (0, –10, –20, and –40°C) also was retrieved from the ERA5 profiles. Isotherm heights delimit the vertical extent of the “charging zone” where graupel, ice crystals and supercooled droplets coexist, allowing significant electrical charging and, ultimately, lightning (e.g., Deierling et al. 2008).

f. Severe-weather reports and fieldwork

Giant hail, together with strong winds, was reported during this event (Fig. 2). We retrieved large-hail reports from (i) the European Severe Weather Database (ESWD; Dotzek et al., 2009), managed by the European Severe Storms Laboratory, and (ii) the Spanish Singular Atmospheric Observation Notification System (SINOBAS; Gutiérrez et al. 2015), operated by AEMET.

These reports include the location, time, and usually the hail size. We combined both data sources and removed duplicate reports, specifically those referring to the same municipality and occurring within a 15-min time window. Finally, we checked the large hail reports by looking at their time and location against radar data, keeping only those that were in areas where the maximum VIL was at least 22.5 mm (the VIL hail threshold set by Rigo and Farnell 2024) or where higher values were within 4 km of the affected area—thus avoiding the removal of reports due to uncertainty in the reported location. Moreover, we adjusted the reported times to be consistent with the observation of the highest VIL values at the reported locations. The final dataset consists of 18 hail reports (15 of which include the maximum hailstone diameter), with a temporal accuracy of ±15 min.

All in all, reports indicated that severe weather occurred between 1200 and 1435 UTC, at a distance of ~115 km, as illustrated in Fig. 2. During the first hour, hail reports indicated sizes ≤5 cm, whereas between 1300–1350 UTC, hail turned gigantic (Table 1). Local spotters published pictures of the hailstones on social media, reporting significant hail damage to roofs, windows, automobiles, and crop fields.

Despite reports of strong convective winds in the media, the previously mentioned databases did not include them for the analyzed event. Fortunately, one of the coauthors conducted fieldwork in the area, commissioned by Spain's public reinsurance company (Consorcio de Compensación de Seguros, CCS), to determine the cause of the damage (i.e., tornado or downburst).

Such data were gathered following the methodology proposed in Rodríguez et al. (2020). The data include a list of locations and photos of each damaged element and the falling direction of uprooted trees. This fieldwork revealed at least one IF1.5 tornado according to the international Fujita scale (IF-scale, ESSL 2023) and three IF2 downbursts (details in Appendix A).

Merging field observations with radar data, we estimated the strong convective-wind events to occur between 1405–1430 UTC. We calculated a damage path of 9.6 km long and 950 m of maximum width associated with the IF1.5 tornado. The vortex start was around 1405 UTC, and it dissipated >10 min later. Moreover, during the damage survey, we detected at least three damaged spots related to IF2 downbursts in the eastward and northeastward directions, along with the tornado track (see Table 1).

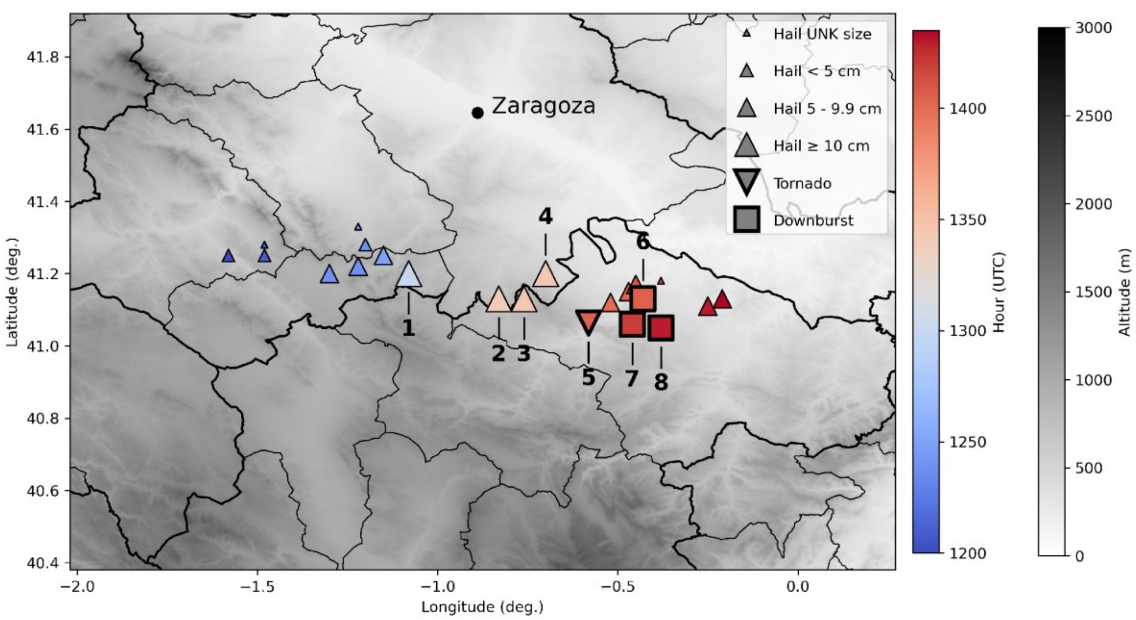

Figure 2: Severe reports (triangles, inverted triangles, and squares represent hail, tornadoes, and nontornadic strong winds, respectively). The color indicates the hour of reports, and in the case of hail, the size of the icon indicates the hail maximum diameter. The ID from the reports corresponds to those listed in Table 1.

Table 1: ID, time (±15 min of uncertainty), phenomenon, diameter (cm, for hail) or intensity (IF, for damaging winds), and damage path characteristics [length (km) and maximum width (m) for damaging winds] from hail ≥10 cm and strong convective-wind reports.

ID	Time (UTC)	Type	Diam. Or Intensity	Damage path
1	1300	Hail	11 cm	
2	1340	Hail	10 cm	
3	1345	Hail	10 cm	
4	1345	Hail	11 cm	
5	1405	Tornado	IF1.5	9.6 / 950
6	1405	Downburst	IF2	2.5 / 1700
7	1420	Downburst	IF2	6.2 / 2600
8	1430	Downburst	IF2	5.0 / 3800

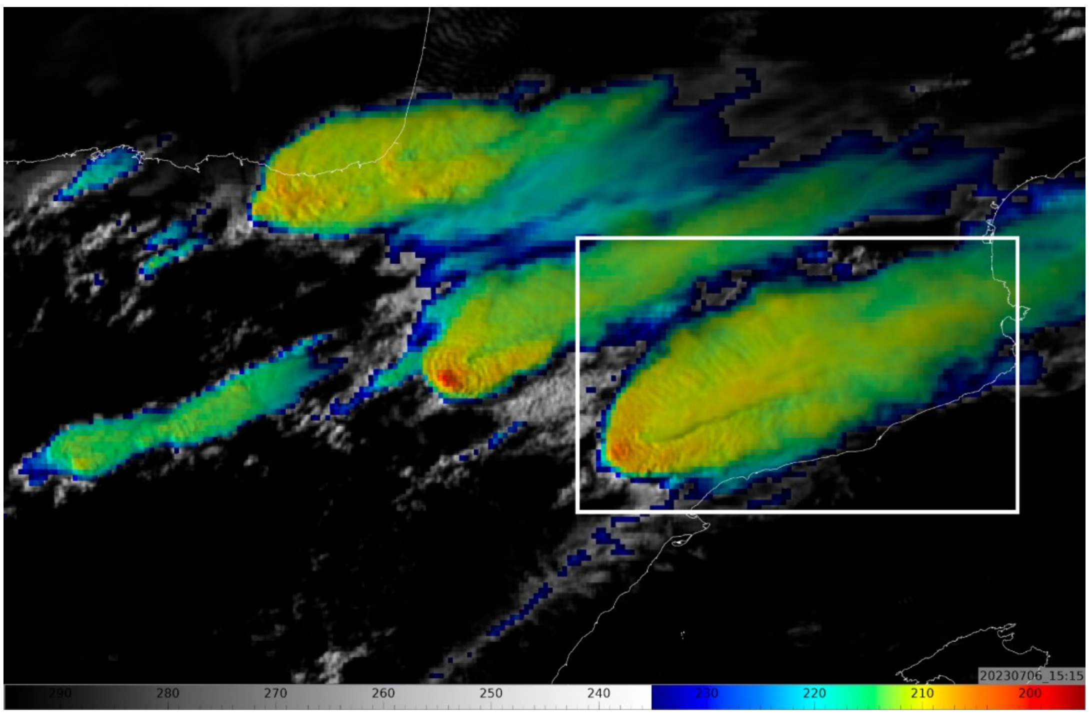

Figure 3: Meteosat blended (or "sandwich," Setvák et al. 2012) product at 1515 UTC. The "sandwich" image combines the high-resolution visible with the color-enhanced thermal infrared (10.8-μm channel) remapped to the same projection and pixel resolution as the high-res visible band. This combination allows us to combine the brightness temperature of the cloud tops (thermal infrared channel) with their shadows and textures. We can locate the storms affecting Vitoria-Gasteiz, Zaragoza, and the case study (framed in white) from north to south and west to east, respectively. *Click image to enlarge.*

3. 6 July 2023 severe-weather outbreak

On 6 July 2023, a severe-thunderstorm outbreak took place in the northeastern Iberian Peninsula. ESWD records showed that between 1200–2100 UTC, large to giant hail, flash floods and strong convective winds affected several locations, causing damage and putting the population at risk. According to Spain's public–private agricultural insurance system, more than 30 000 insured hectares of field crops were damaged by severe thunderstorms on that day (Agroseguro 2023). For instance, in the city of Vitoria-Gasteiz (in the northern part of the affected area), large hail caused head contusions to at least 11 people, and flash floods were reported in the city of Zaragoza. The Meteosat "sandwich" product at 1515 UTC depicts the outbreak of severe thunderstorms in Fig. 3. We focus our analysis on the Mid Ebro Valley

(Fig. 1), south of Zaragoza, where the largest hail recorded (ø >10 cm) together with damaging winds (i.e., an IF1.5 tornado and three IF2 nontornadic events).

a. Synoptic framework

The synoptic framework from 6 July 2023 at 1200 UTC was characterized by a ridge at 500hPa extending from North Africa to the central Mediterranean and a low located to the northwest of Ireland, providing southwest flow over Europe at mid and upper levels (Fig. 4). In this regard, a 300-hPa southwesterly wind maximum was affecting the region of interest. The area where the thunderstorm developed was on the trailing flank of the ridge. At the surface, a pressure low (<994 hPa) was located west of Ireland, whereas high pressures (>1018 hPa) were located over central Europe and the Atlantic. Additionally, a thermal pressure low was present over the Iberian Peninsula due to daily heating.

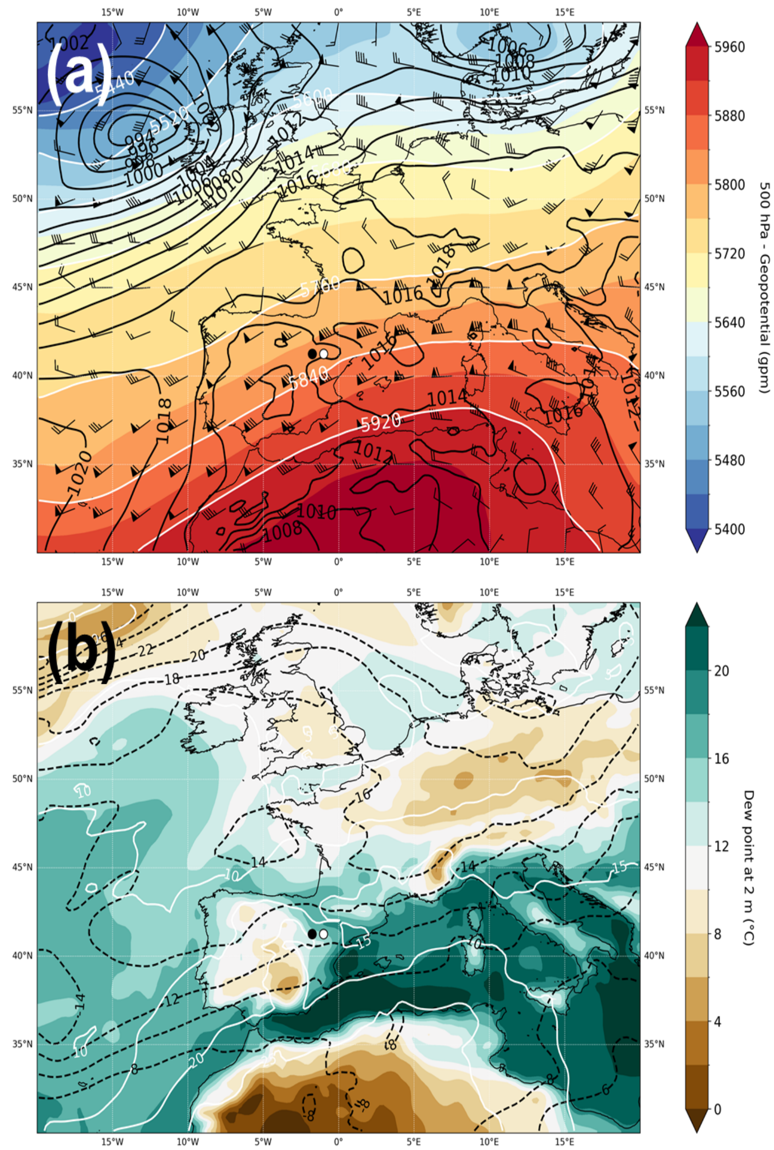

Figure 4: Maps from 6 July 2023 at 1200 UTC of: a) 500-hPa height (white lines and color shaded), mean sea level pressure (black lines) and 300-hPa wind (wind barbs), and b) 2-m dewpoint (color shaded), 850-hPa temperature (white lines) and 500-hPa temperature (black dashed lines). The black dot indicates the location from which the preconvective pseudo sounding (11 UTC; Fig. 5a) was retrieved, whereas the white dot denotes the gridpoint corresponding to the pre–giant hail pseudo-sounding (1300 UTC; Fig. 5b). *Click image to enlarge.*

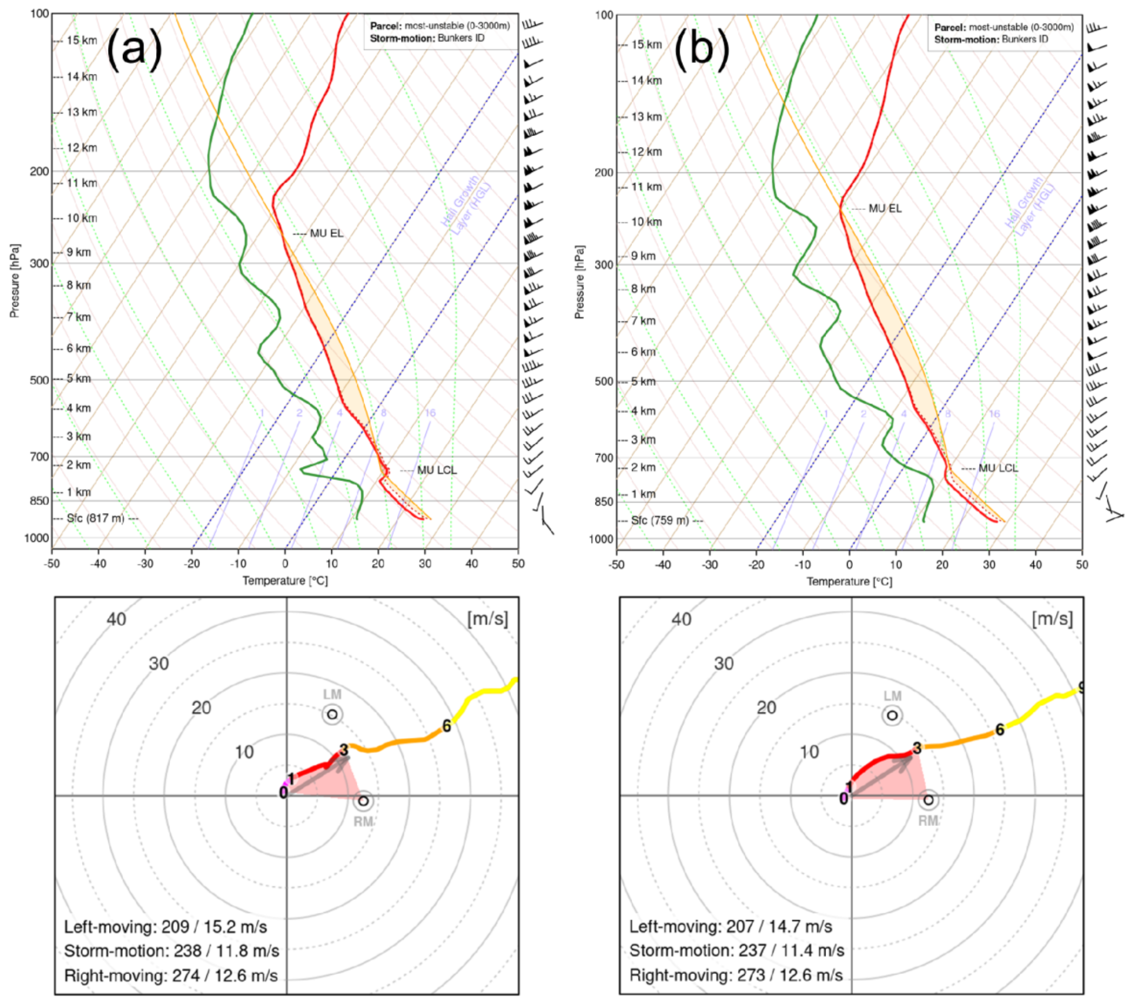

Figure 5: ERA5-retrieved profiles from a) 1100 UTC (preconvective environment) and b) 1300 UTC (i.e., before giant hail and strong winds in the central part of the thunderstorm track). *Click image to enlarge.*

At 500 hPa, a thermal wave was moving eastward, whereas at 850 hPa, the temperature was rising due to daily heating, producing an increase of vertical temperature lapse rate. At 1200 UTC, in the area of interest (marked with a white dot in Fig. 4), the temperature was –12°C and 17°C at 500 and 850 hPa, respectively. Furthermore, the Iberian thermal low favored a Mediterranean southeasterly flow at low levels in the Ebro valley, resulting in an increase of the dewpoint (at 2 m) and therefore, an increase in the water-vapor content (Fig. 4b). These conditions were conducive to deep moist convection and, along with the topographic forcing from the Iberian System (the western Ebro Valley Mountain range with peaks reaching 2300 m MSL), facilitated convective initiation.

Previous studies have identified similar summer synoptic frameworks in this region associated with both deep, moist convection and severe-weather events. Several supercells (see weather types 7 and 10 in Calvo-Sancho and Martín 2020), hailstorms (SWT pattern in Aran et al. 2011; the 31 July 2015 event in de Pablo Dávila et al. 2021; Calvo-Sancho et al. 2022), and tornadoes (circulation weather type “2+” in Rodríguez and Lemus-Cánovas 2023) have been reported in the Ebro Valley under comparable synoptic patterns. These events are typically associated with the interaction between zonal circulation, an eastward-propagating thermal wave, and the presence of a thermal low over the Iberian Peninsula.

b. Thermodynamic vertical profile

Here, we analyze the vertical temperature, humidity, and wind profiles to assess the pre-convective environment and the thermodynamic

Table 2: Altitude (MSL) of environmental isotherms 0, –10, –20 and –40°C at 1100 UTC (preconvective environment) and 1300 UTC (i.e., before giant hail and strong winds), according to pseudosounding retrieved from ERA5.

ISOTHERMS / ALTITUDE (km MSL)	1100 UTC	1300 UTC
0°C	4.1	4.2
– 10°C	5.3	5.5
– 20°C	6.9	7.0
– 40°C	9.6	9.7
Equilibrium level (EL)	10.6	11.1

and kinematic conditions previous to the giant hail and strong winds (reports in Table 1). An ERA5-retrieved profile previous to convection initiation, and for the closest grid point, showed an adiabatic evolution at low levels (Fig. 5a). The 1-km LR was superadiabatic (11.5°C km^{-1}), and the mean value at midlevels (3–6 km) was 7.2°C km^{-1},providing instability. Despite the low surface dewpoint (11–12°C), most-unstable CAPE presented moderate values (800–900 J kg^{-1}) favoring deep, moist convection. The LCL was relatively high (1.8 km AGL) due to the low-level dry air, whereas the EL reached 9.7 km AGL, providing 7.9 km of CCD.

The altitude of significant isotherms (0, –10, –20, and –40°C) had similar values before the convection initiation (11 UTC) and just before giant hail was reported (13 UTC), with a slight increase of about 100–200 m in the latter case (Table 2). On the other hand, the EL height rose from 10.6–11.1 km, according to both ERA5 pseudo soundings. Note that these values are above sea level (MSL).

Two hours later (1300 UTC), at the grid point closest to the central part of the thunderstorm track and prior to the main severe-weather reports, the ERA5-retrieved profile showed a similar evolution in temperature and dewpoint. However, both values increased at the surface (Fig. 5b) due to the daily heating and moist advection by low-level southeasterly winds in the Ebro Valley. Therefore, the most-unstable CAPE rose to 1000–1100 J kg^{-1}. The LCL (2.0 km AGL) and the EL (10.4 km AGL) both increased, especially the latter, which led to a CCD of 8.4 km. Deep, moist convective conditions were enhanced, and the steep sub-LCL superadiabatic lapse rate indicated a favorable environment for severe convective winds (Taszarek et al. 2020).

Both vertical profiles show weak southeasterly winds that rapidly shifted to more intense southerly and southwesterly directions at 850 and 800 hPa, respectively. This evolution provides strong (28–29 m s^{-1}) and moderate (from 12 m s^{-1} for the first pseudo sounding up to 15 m s^{-1} for the second) environmental wind shear for the 0–6-km (DLS) and 0–3-km layers (MLS), respectively. These conditions, along with thermodynamic parameters such as moderate to large CAPE and steep LR at low and middle levels, can support supercell formation (Thompson et al. 2003), large to giant hail, and strong winds (Taszarek et al. 2020). Combined parameters such as WMAXSHEAR03, which increased from 500 m^2 s^{-2} to 670 m^2 s^{-2}, also demonstrated conditions prone to tornadogenesis (i.e., WMAXSHEAR03 >500 m^2 s^{-2}) (Rodríguez and Bech 2021).

Hodographs presented a straight shape due to low-level weak winds and the lack of directional wind shear from 800 hPa (Fig. 5). Though straight hodographs are less frequently associated with mesocyclonic tornadoes (Nixon and Allen 2022), they are favorable for large hail (Kumjian et al. 2021). Moreover, straight hodographs favor storm splitting where both right- and left-moving storms survive (Klemp and Wilhelmson 1978; del Moral et al. 2020), as it is shown in the next section. According to the preconvective ERA5 profile, the mean storm motion vector was 12 m s^{-1}, 238°, whereas for the right-moving supercell vector was 13 m s^{-1}, 274° and for the left-moving vector was 15 m s^{-1}, 209° (Bunkers et al. 2000).

4. Temporal evolution

a. Period 1: First development, splitting and "lightning hole" (1120–1315 UTC)

Figure 6 shows the time series for radar and lightning data, along with severe-weather signatures and reports. Radar scans reveal the first reflectivity echoes (ZMAX >25 dB*Z*) at 1120 UTC, ~110 km southwest of the radar site. The initial cell moved roughly in the direction of the mean storm motion (mainly dominated by mid- and upper-level winds), southwest to northeast. Sustained deep convection resulted in reflectivity cores >40 dB*Z* 30 min later. At 1200 UTC, TOP-15 attained an altitude of 13 km MSL, while ZMAX recorded a value of 60 dB*Z*, indicating an increase of >30 dB*Z* within a 40-min interval.

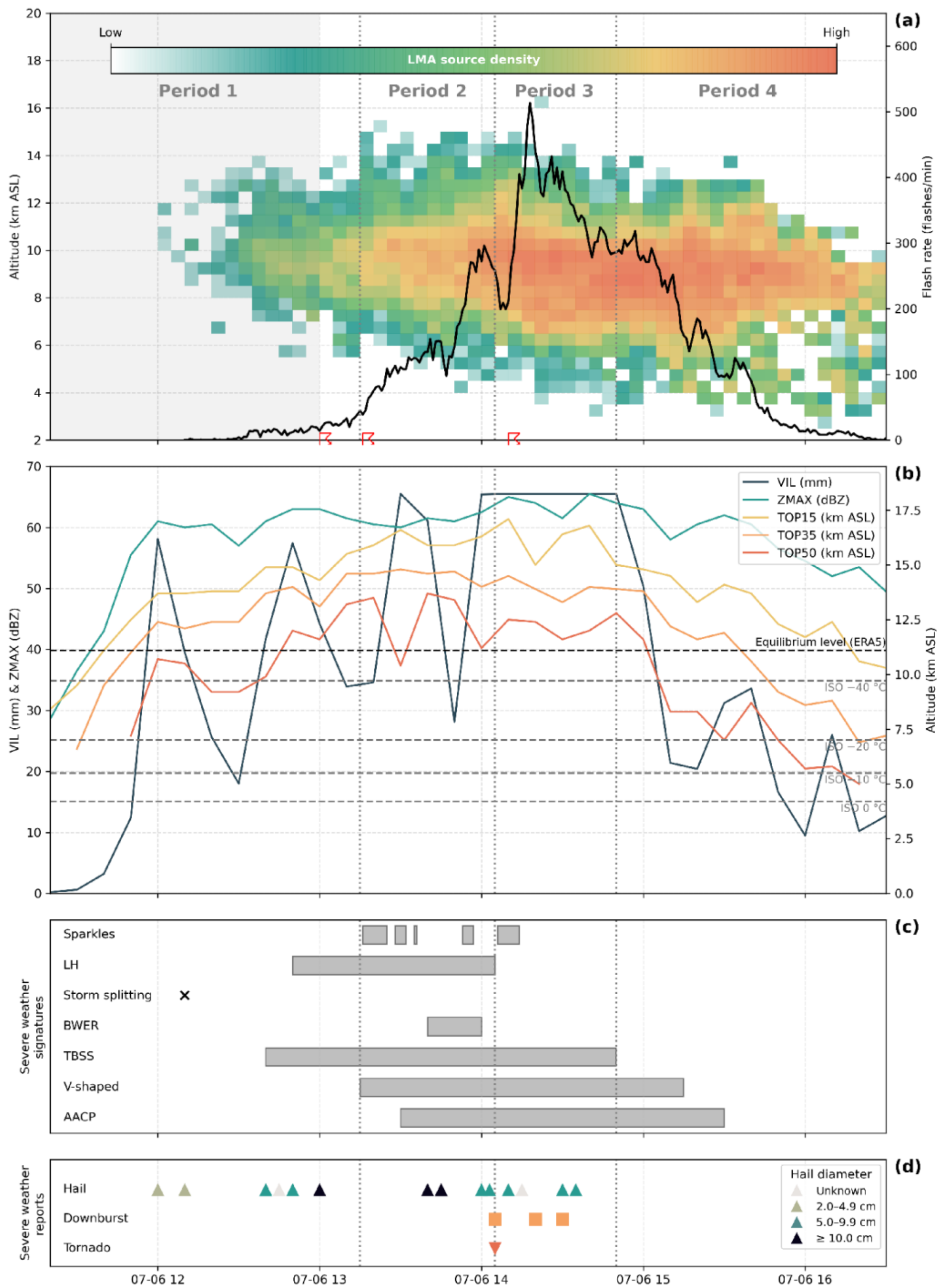

Figure 6: Time series from 1120–1630 UTC of the right-moving storm showing: a) the normalized density of total LMA sources per flash, accumulated in 5-min × 500-m time–height bins according to the flash initiation location (shaded) and LMA flash rate (min^{-1}). Lightning jumps are indicated with red ☈ symbol. Notice that the time period when LMA data is considered not reliable for coverage reasons is shaded in grey. In b) echo-top heights (TOP-15, TOP-35 and TOP-50, in km MSL) are shown, with maximum reflectivity (ZMAX, dB*Z*) and vertically integrated liquid (VIL, mm). Altitudes of the 0°C, −10°C, −20°C, and −40°C isotherms and the equilibrium level retrieved from ERA5 (at 1300 UTC) are added. c) Severe-weather signatures [sparkles, lightning hole (LH), storm splitting, BWER, TBSS, V-shaped cloud top, and above-anvil cirrus plume —AACP—). d) Severe-weather reports (hail, downbursts, and tornado). *Click image to enlarge.*

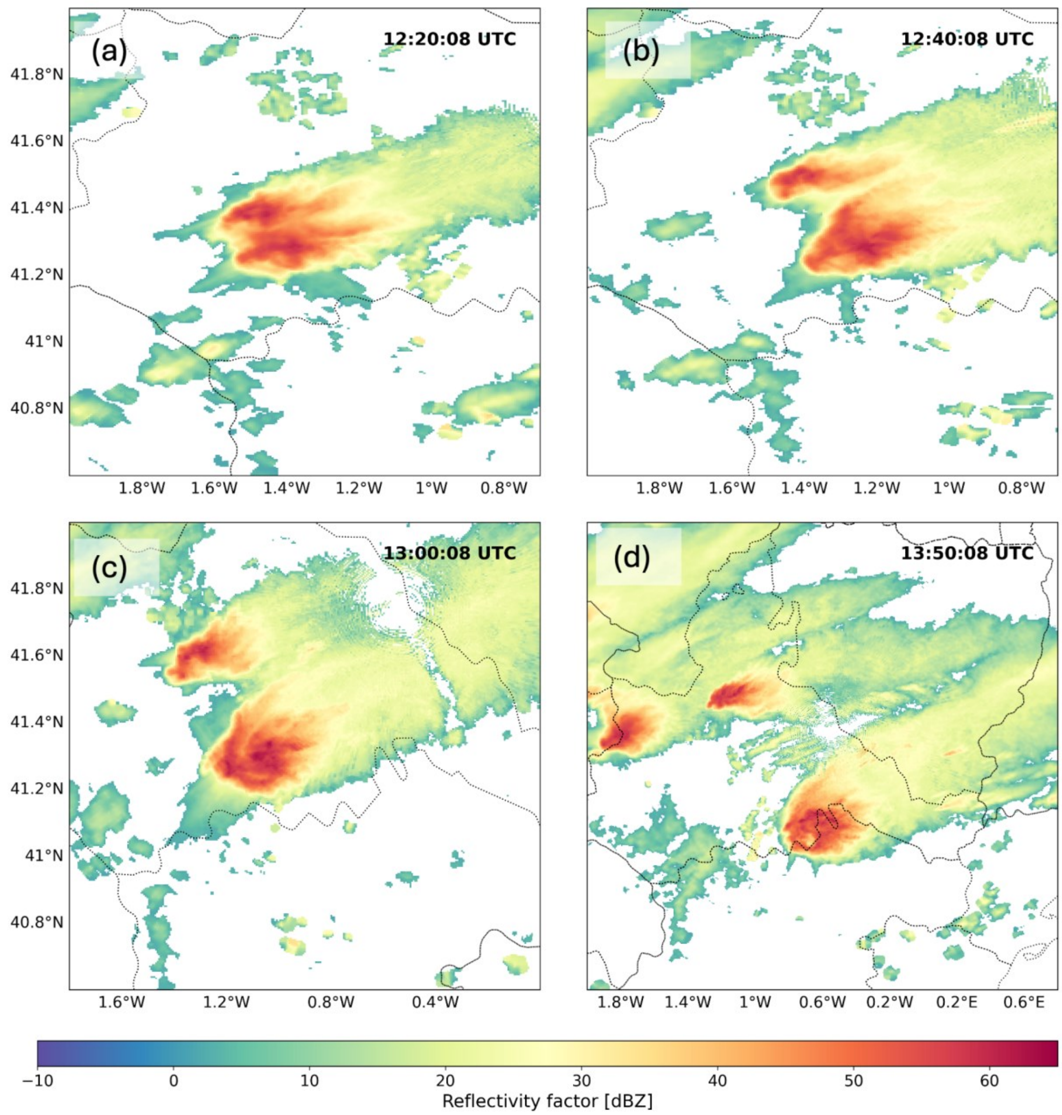

Figure 7: Zaragoza radar maximum reflectivity product, ZMAX, in dB*Z*, is depicted at the following times: a) 1220 UTC; b) 1240; c) 1300; and d) 1350, respectively. The cell splitting started around 1220 UTC (a), with the left mover moving north and the right mover moving southeastward (b and c). The left-mover did not develop further, merging with another cell 2 h later (d). Contrarily, the right-mover developed into a long-lasting supercell.

The 1210 UTC radar scan indicated initial evidence of cell splitting, with the left mover shifting northward and merging with another cell 2 h later (Fig. 8). Storm splitting, a part of supercell evolution (Davies-Jones 2014), is an early sign for the forecaster in surveillance tasks. The right mover—the focus of this study—began to deviate toward the southeast. The splitting caused a momentary decrease in the radar series, particularly in the VIL product. After the VIL recovery (>40 mm), several images in the radar sequence showed a linear echo characterized by a TBSS, manifest as weak radar reflectivity values extending down-radial from areas of intense mid-level reflectivity.

The TBSS indicates the presence of large hail, and hailstones with diameters of 5–9 cm were reported at ground level during this period (Fig. 6d). This feature is observable in several images of the radar sequence between 1240 and 1450 UTC (e.g. Figs. 7 and 10), >2 h during which radar reflectivity is very high at medium levels, with TOP-50 altitudes ranging from 10–14 km MSL during this interval.

Despite the rapid development indicated by the radar products (e.g. TOP-50 close to the EL at 1300 UTC, Fig. 5a), and thus expecting frequent lightning activity (e.g., Salvador et al., 2021), no LMA sources were detected until 1155 UTC (≈160 km from the center of the network). LMA detections remained infrequent until 1230 UTC (≈140 km) (Fig. 8). This low activity suggests that the LMA network exhibited low sensitivity during the initial period (see Appendix B for details on LMA efficiency).

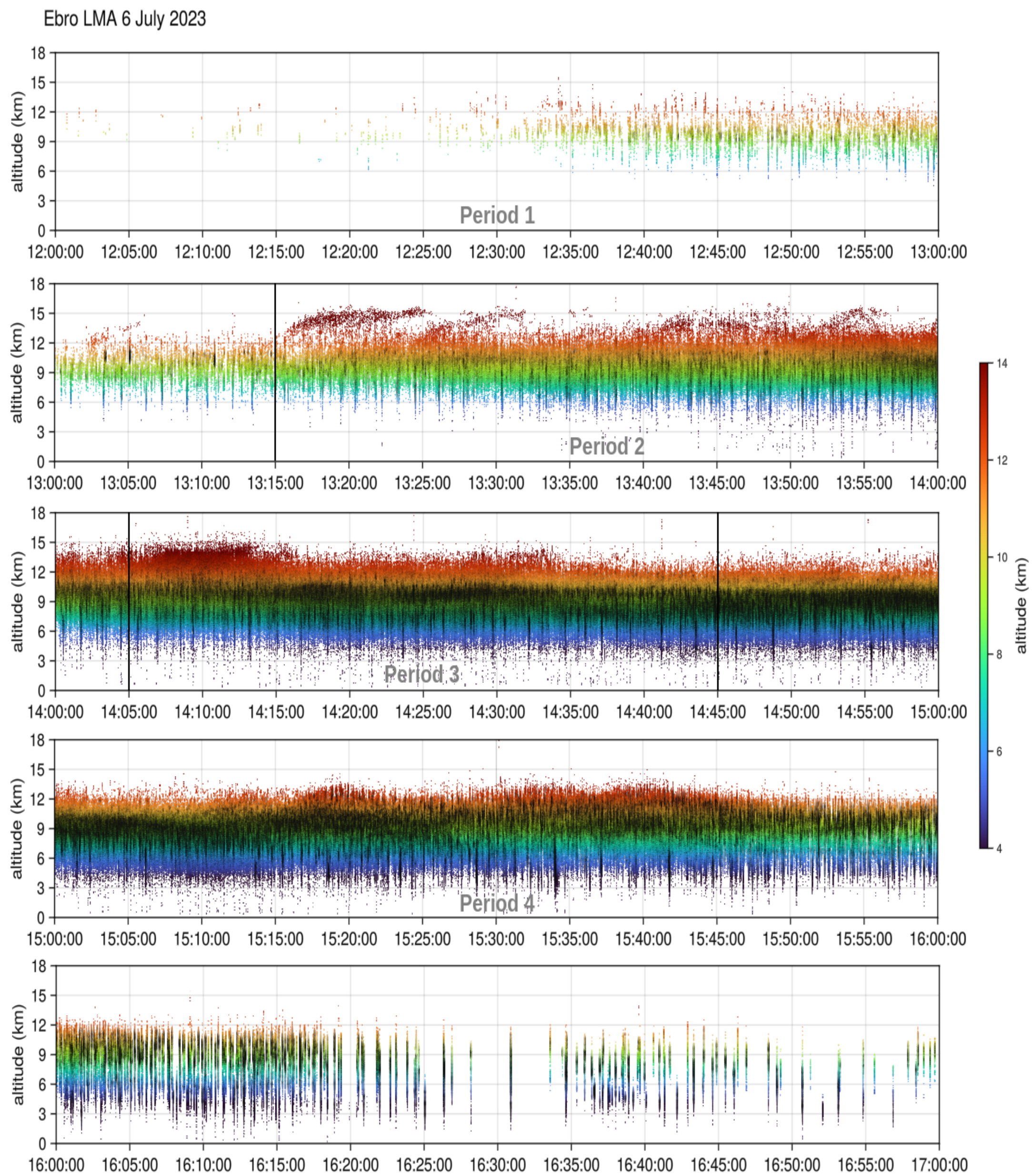

Figure 8: Time series of overall lightning activity. Altitude MSL vs. time of VHF sources mapped by the LMA along the storm lifecycle (colored by altitude, colors darken as density of sources increases). Individual vertical line-like features denote individual flashes at development and decay stages; during maturity, lightning activity becomes so frequent that individual lightning flashes are hard to distinguish within the continuous filling source detection by the LMA. The four periods into which the storm evolution was divided are indicated by vertical black lines.

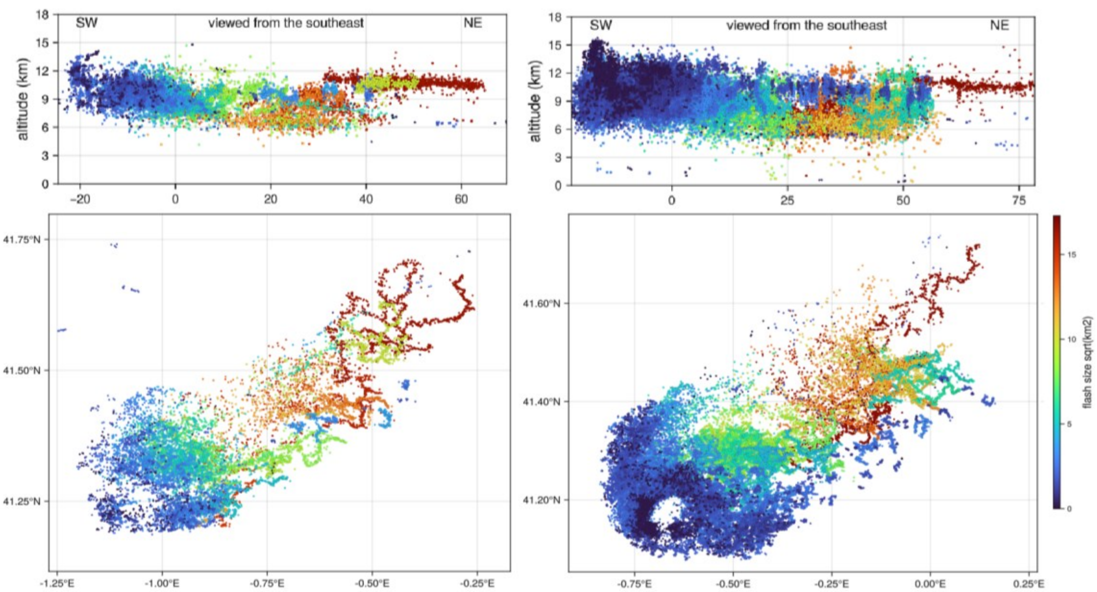

Figure 9: Two stages of the lightning-hole signature: 1300–1310 UTC (left) and 1350–1355 UTC (right). This information is viewed through the LMA flash size, presented in both the plan view (bottom panels) and the altitude MSL by longitude from the southeast (top panels). 0.1° in latitude equals ≈11 km; the activity in the supercell extends 80 km in maximum length and 40 km wide. At 1350–1355 UTC (right panel), the lightning hole has a diameter of ≈7 km. *Click image to enlarge.*

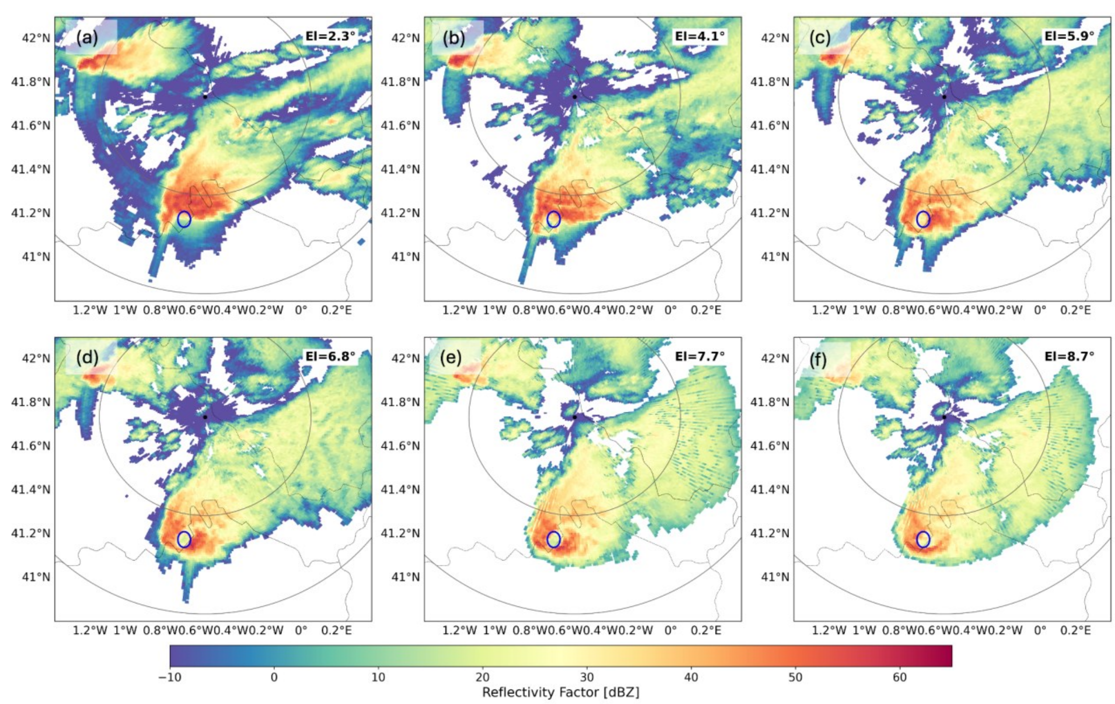

Figure 10: Reflectivity factor (dB*Z*) at 2.3°, 4.1°, 5.9°, 7.7°, 6.8°, 8.7° elevation angles at 1350 UTC 06 July 2023. The hook echo at lower elevations transforms to the ring or doughnut shape at mid-elevations, representing the BWER. Dotted grey lines display the 50- and 100-km range rings, while a black dot indicates the radar location. The blue circles indicate the lightning hole identified at that time based on LMA data. *Click image to enlarge.*

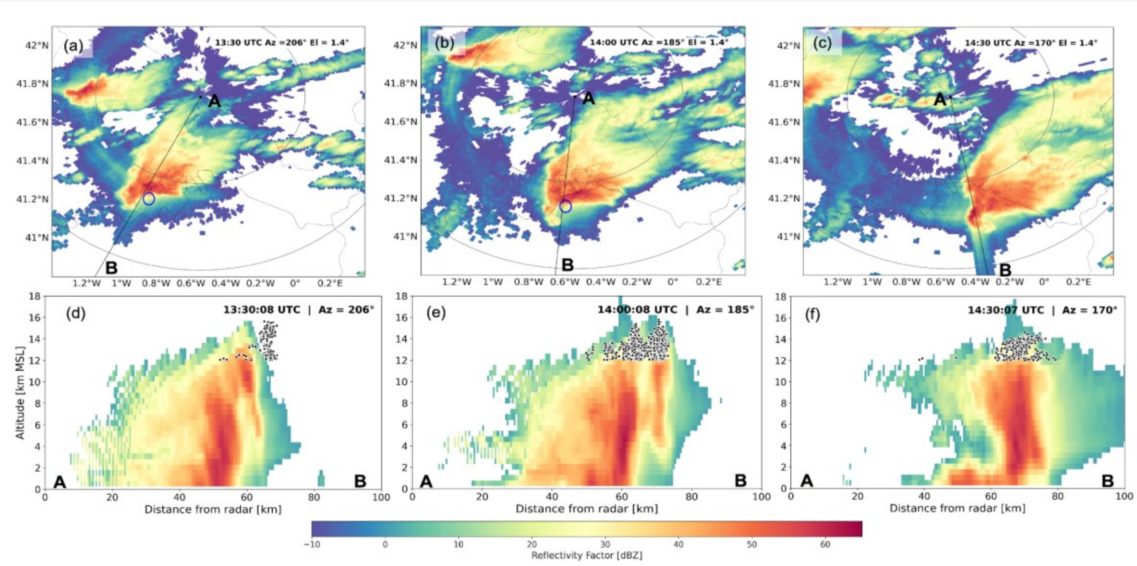

Figure 11: Reflectivity factor (dB*Z*) at 1.4° elevation angle (upper panels) at: a) 1330 UTC, b) 1400 UTC, and c) 1430 UTC; and cross sections (bottom panels) indicated with the A-B transect along the d) 206°, e) 185°, and f) 170° azimuths. Radar location and 50- and 100-km range rings are displayed. The blue circles in (a) and (b) indicate the lightning hole identified at that time based on LMA data. The cross section (in a and b) depicts a clear BWER. "Sparkles" detected by the LMA are overlaid to the cross sections in (d,e,f). In (c), we can observe a double TBSS signature both along the transect direction. A well-defined hook echo is present at that timestep. The same pattern can be seen in (f), represented with reflectivity values around 10 dB*Z* in the radial direction from the radar and behind the main cell core (above the B letter). The BWER is also visible in this cell stage. *Click image to enlarge.*

At ≈1250 UTC, a lightning "hole" or "ring" appeared in the LMA (Fig. 9). This region devoid of lightning activity indicates short residence times for charging, due to the strong updraft (e.g., Krehbiel 2000; Emersic et al. 2011; Calhoun et al. 2013). Based on the top-down perspective of a traditional supercell (Lemon and Doswell 1979), the hole aligns with the main updraft (Fig. 10). The hole persisted for ≈75 min, expanding to a maximum diameter of 7 km, before disappearing around 1405 UTC. The lightning hole traversed the depth of the thunderstorm, only being hindered later by momentary activity at the overshooting top (Fig. 13).

b. Period 2: Updraft intensification, maximum vertical development and "sparkles" (1315–1405 UTC)

This period started with a lightning jump (1318 UTC, Fig. 6a), along with overshooting lightning and the V-shaped signature in METEOSAT imagery, indicating the strengthening of the updraft. The storm attained its peak development with TOP-15 around 17 km MSL and VIL rapidly increasing to values above 60 mm, indicating the presence of large hail (Edwards and Thompson, 1998). During this period, massive hailstones (ø >10 cm) were observed at ground level. The intense updraft responsible for the lightning hole was similarly evident in radar images (1340–1400 UTC), exhibiting a noticeable reflectivity minimum (BWER) in the same area (Fig. 10). The BWER can be seen at different elevation angles at 1350 UTC (Fig. 10).

As often observed in supercells, the lightning hole coincided with the BWER (e.g., MacGorman et al., 2005; Wiens et al., 2005). Reflectivity within the hole remained <40 dB*Z*, indicating that the central region of the lightning hole lacked significant concentrations of large ice particles but contained supercooled liquid water (SLW, Chmielewski et al. 2020). The reflectivity values surrounding the hole reached values >60 dB*Z*. During this period, TOP-15 heights around the "hole" reached 17 km MSL.

(a)

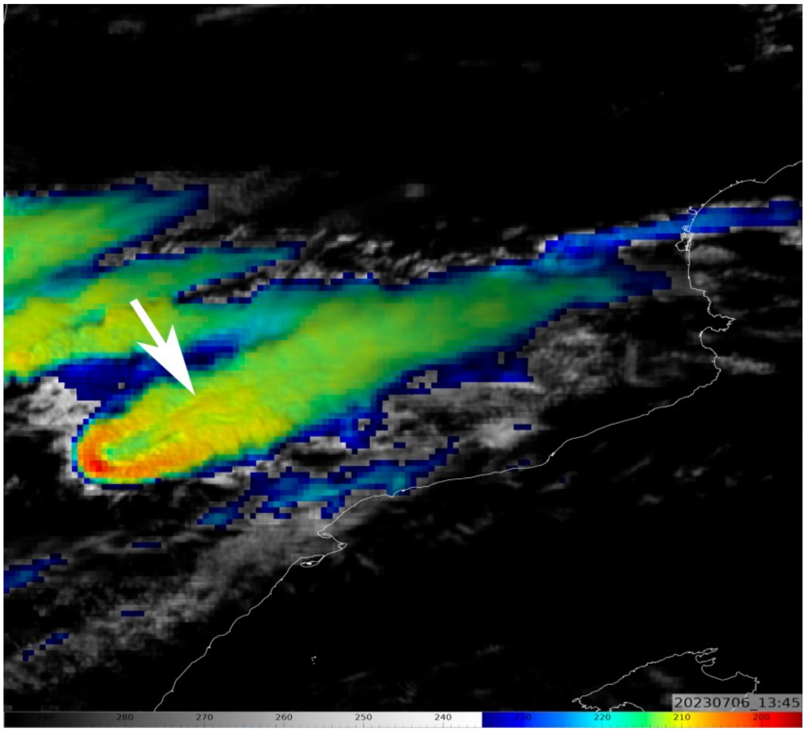

(b)

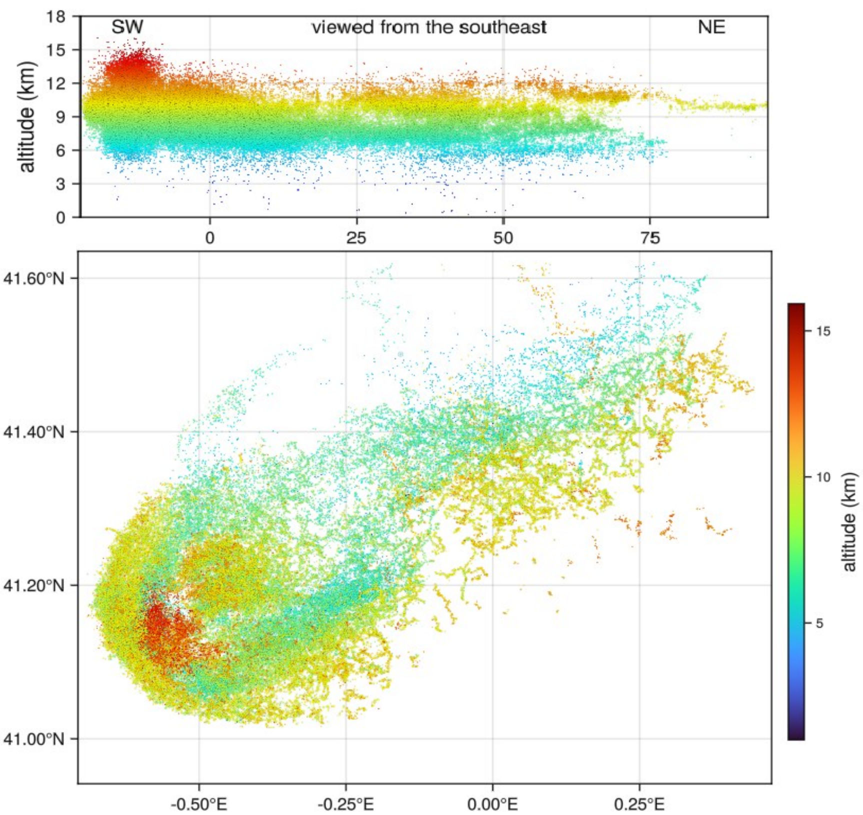

Figure 12: a) Meteosat blended (or "sandwich"—Setvák et al., 2012) product like in Fig. 3 at 1345 UTC (left panel) and b) LMA altitude-colored VHF sources from 1345–1350 UTC, presented in both the plan view (bottom panel) and the altitude by longitude from the southeast (top panel). In the satellite image, the white arrow indicates the anvil cirrus plume above. *Click images to enlarge.*

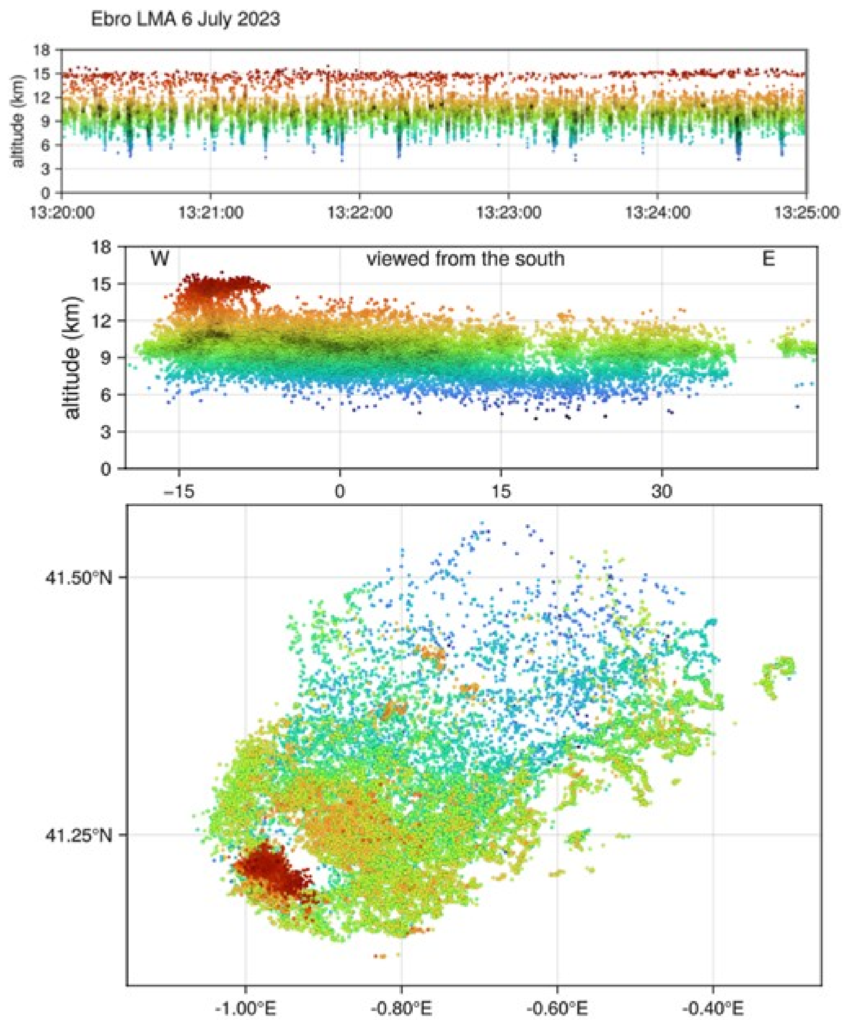

Figure 13: Multipanel display of 5 min of sources (1320–1325 UTC) detected by the LMA. The top panel is altitude MSL (km) versus time (s). The bottom panel is a plan view map (0.1° latitude equals 11.1 km). The mid panel shows altitude (km) by longitude (view from the south). Heights of the very high frequency sources are colored with altitude, showing the sparkles above the lightning-hole signature. *Click images to enlarge.*

Another way to identify the BWER is with radar vertical cross-sections: Fig. 11 shows the lower-reflectivity column that formed the BWER at different times, extending to the cloud top.

Additionally, in this period, Meteosat imagery showed the first signs of the V-shaped feature (Maddox 1981; McCann 1983; Adler and Mack 1986) (Fig. 12). The V-shaped formation occurs when powerful updrafts of the storm cause clouds to extend into the lower stratosphere, crossing the tropopause, resulting in overshooting tops (OT, Heymsfield and Blackmer 1988). Heavy rain (Negri and Adler 1981), turbulence (Lane et al. 2003), and tornadoes (Bedka 2011) have been associated with OTs. This stratospheric intrusion obstructs high-altitude winds, compelling them to diverge around the overshooting, which results in a depression downwind (Fujita 1978). Interestingly, altitude-colored VHF sources mimic the V-shaped structure as shown in the right panel in Fig. 12. While OTs are usually short-lived (~0.5 h, Bedka et al. 2010), in the present case study, the V-shaped signature was well defined for 2 h (1315–1515 UTC). Additionally, a cirrus plume can be observed above the main cumulonimbus anvil in the Meteosat sequence, caused by strong updrafts pushing through the tropopause and breaking gravity waves (Fig. 12). This signature, called "above anvil cirrus plume" (AACP), has been reported during severe-weather events (Bedka et al. 2018). In the present case, AACP was detected from 1330–1530 UTC, after the first giant hail report but before damaging winds, similarly to the V-shape. After this period, some cirrus associated with AACP persisted temporarily.

Figure 8 illustrates lightning increasing during this period, as the LMA flash occurrence became continuous and volume-filling (Krehbiel 2002). Moreover, strong convective surges began between 1316–1325 UTC, with LMA sources reaching 15 km MSL in height, signaling the intensification (Krehbiel 2002). The majority of lightning initiations remained above 10 km MSL during all this period (not shown), around temperatures of –40ºC, another signal of the continued strength and size of the updraft (Zhang et al. 2017; Mecikalski and Carey 2018).

This first period of lightning in the overshooting tops occurred after the TOP-15 reached 15 km MSL and coincided with a sudden increase in the radar height of the TOP-50 in the rear flank of the mesocyclone, which jumped from 10 to 13 km MSL in 30 min (1240–1310 UTC). Similarly, it ended when the height of the TOP-50 in the radar sequence decreased below 12 km MSL (whereas the TOP-15 stayed above 15 km MSL until 1450 UTC). A closer look shows that this upper lightning activity consists of isolated VHF sources, suspended 2 km above the bulk of the lightning occurring at the core of the storm (Lyons et al. 2003; MacGorman et al. 2017). This activity shows a steady rate and looks like an upper "band" of VHF radiation in the time vs. height panel of Fig. 13. The first sparkles lasted for around 10 min (1316–1325 UTC), and other episodes followed (1326, 1341, and 1353 UTC).

Detailed analysis showed isolated bursts, not developing into full lightning channels, as observed in other cases (e.g., Chmielewski et al. 2018). This behavior has been described as lightning bubbles by Ushio (2003), which may be akin to the “sparkles” observed in subsequent, more sensitive LOFAR (low-frequency array) studies due to their intermittent nature (Scholten et al. 2023), noticing the connection to high turbulence in the updraft's overshooting region, where mixed charge layers trigger the sparkles. In plain view, these sparkles cluster above the lightning hole, slightly shifted to the rear flank (see Fig. 13). Such a pulsating behavior may indicate updraft cycles (e.g., Krehbiel 2002, MacGorman et al. 2017).

Figure 6 reveals a cyclic pattern in VIL that is consistent with surface observations of large hail. Two of these events occurred within Period 2 (1315–1405 UTC) and coincided with the detection of sparkles. This temporal correspondence indicates that sparkles and increasing VIL may be linked to an intensification of the updraft preceding hailfall at the surface. Along similar lines, Van den Broeke and Green (2024) documented repeating storm cycles in which increasing storm-relative inflow were found to precede updraft strengthening and subsequent hailfall on the ground, after a short delay.

c. Period 3: End of the hole, peak in the flash rate and tornadogenesis. (1405–1450 UTC)

This period started with another lightning jump (1412 UTC, Fig. 6a), which led to a sharp peak on the flash rate at 1418 UTC (500 flashes min^{-1}). This lightning jump is related to an increase in VIL value, as well as to a decrease in echo tops (e.g., Metzger and Nuss 2013). The period’s transition is also marked by the BWER collapse, the end of the lighting hole and the first reports of a tornado. Sharp (2005) noted that the BWER collapsed around the same time as the tornado began. From this point, charge regions gradually subsided (Fig. 6a), and the lightning-initiation median height steadily decreased from 10 to 9 km MSL at the end of the period. Steiger et al. (2007) also observed lightning heights to decrease before tornadogenesis, as well as a weakening of radar characteristics during that process. However, in the present case study, radar characteristics related to the storm’s height (TOPS- 15, 35 and 50) kept similar values compared to the previous period, only to decrease in the final period. Moreover, VIL reached its maximum during this period (>65 mm).

In this third period, overshooting discharges were maintained more steadily (1405–1413 UTC), as ZMAX was above 60 dB*Z* and VIL remained above 60 mm for 50 min (1400–1450 UTC), whereas overshooting sparkles pulsed in the second period in response to the pulses in the storm’s updraft (Ushio et al. 2003). A similar behavior was reported by DiGangi et al. (2016)

in the 2012 May 29 Kingfisher, OK, supercell. METEOSAT imagery kept showing the V-shaped and AACP signatures during this third period.

d. Period 4: Dissipation, downdraft is the predominant flow (1450–1620 UTC)

After 1450 UTC, radar values and lightning flash rate decreased gradually, indicating that the downdraft was the predominant flow. With the sharp decrease in VIL, the TBSS signature disappeared from radar scans after >2 h of almost continuous presence. Despite the gradual decrease after its peak (1418 UTC) the flash rate kept above 300 flashes min^{-1} until 1500 UTC, when the abrupt decay of the TOP-50 sharpened the flash-rate drop. In parallel, LMA source density (Fig. 6a) shows a steady decline in the flash heights. Despite the gradual decrease of the flash rate, some surges still could be observed around 1520 and 1535 UTC (Fig. 8), although they did not produce overshooting lightning. Compared to period 2, Fig. 8 shows many more VHF sources in period 4, with lightning being less frequent but larger. Very large flashes spread to the anvil region (e.g., Kuhlman et al. 2009; DiGangi et al. 2020). METEOSAT severe-weather signatures (V-shaped, AACP) were the last to disappear, as TOP-15 finally went below 14 km MSL height.

5. Discussion

a. The lightning hole: A severe-weather signature

Why do some supercells exhibit a lightning-hole signature? In the early 2000s, the advent of LMA systems led to the observation of a lightning hole in the core of the updraft. Krehbiel et al. (2002), MacGorman et al. (2005), Payne et al. (2005), Steiger et al. (2007), and Calhoun et al. (2013, 2014), among others, have examined the physics behind the formation of lightning holes in supercells. Lightning holes have been observed during tornadic supercells with LMA systems in the STEPS (Lang et al., 2004; MacGorman et al. 2005) and TELEX (MacGorman et al. 2008) campaigns. Lang et al. (2004) were the first to associate the lightning hole with the BWER. MacGorman et al. (2008) deduced that the lightning hole likely formed for reasons analogous to the existence of the BWER in the radar: the brief residence time within the mixed-phase region, attributed to a rapid updraft, would result in a relative lack of precipitation and microphysical charging from rebounding collisions between riming graupel and cloud ice. Following the analogous terminology for the BWER, Ziegler et al. (2014) named it “bounded weak lightning region” (BWLR).

After the STEPS and TELEX campaigns, different simulations have been able to reproduce the lightning hole on the Geary supercell (e.g., Calhoun et al. 2014; Ziegler et al. 2014). Ziegler et al. (2014) used the NSSL three-dimensional COMMAS cloud model. The authors claim to have validated the lightning hole’s link to areas within the supercell storm characterized by weak hydrometeor particles that undergo minimal or no charging during their paths. Simulations by Calhoun et al. (2013, 2014) show that the lightning hole or BWLR forms when the vertical velocity in the updraft zone exceeds 40 m s^{-1}. As a result, a decrease in charging occurs in the region due to the lack of rebounding collisions between riming graupel and cloud ice, reducing the number of particles accessible for the non-inductive charge mechanism (NIC, Takahashi 1978).

Typical durations for the lightning hole are about 15–20 min (e.g. MacGorman et al. 2005) whereas in the present case study it lasted for >1 h. The hole is often capped by a mantle of overshooting lightning (Chmielewski et al. 2020), which can partially hinder the signature and challenge its visual detection. In the present case study, the "hole" extended beyond mid-layer altitudes, forming a free-lightning chimney that spanned the entire height of the column, as shown in Fig. 9, later on covered by overshooting lightning (e.g. Fig 13). Other studies (e.g., Zhang et al. 2004; McKinney et al. 2009) have observed holes extending throughout much of the storm depth. Combined with its long duration, this signature suggested the presence of a strong and steady updraft, as the classical conceptual model of a supercell indicates (Lemon and Doswell 1979).

LMA data in the present case study revealed that the lightning hole was collocated with the BWER pattern detected in the radar volume (Figs. 10 and 11), showing rather low reflectivity values compared to its external ring. This suggests that the BWER predominantly consists of SLW (e.g., Williams et al. 2005; Bruning et al. 2010; Chmielewski et al. 2020). Due to insufficient time for graupel and small hail to develop within this strong updraft zone, the likelihood of electrical charging and hence lightning is absent. Contrarily, the greatest charge separation occurs at the periphery of the updraft where turbulence creates small pockets of charged particles (Bruning and MacGorman 2013; Calhoun et al. 2013). These small pockets of charge favor frequent, small flashes that are constrained in areal extent by the small size of the charge regions the flash propagates through (e.g., Payne et al. 2010). In the present case study, this can be observed in Fig. 9.

b. Large-hail wet growth

According to Emersic et al. (2011), the “wet growth” of large hail could also explain the formation of a lightning hole without a mesocyclone. Under wet-growth conditions, graupel and hail particles become heavily coated with liquid water, decreasing the number of effective rebounding collisions and setting unfavorable conditions for NIC separation (Saunders and Brooks 1992). Jayaratne and Saunders (2014) demonstrated that wet growth results in an order of magnitude smaller charge separation than dry growth. Assuming wet growth, contrary to the BWER shown in the radar, the lightning hole would be associated with large values of reflectivity, which was not the case. Whatever the origin, either explanation would preclude NIC separation. All in all, the presence of a lightning hole (in the core of the updraft) indicates severe weather, regardless of its direct link to a BWER (Murphy and Demetriades 2005).

c. Presence of a mesocyclone

The analysis of the radar base velocity images is the most used technique to detect the presence of a mesocyclone. Unfortunately, Quirantes et al. (2014) contend that the AEMET Doppler radar network, which includes the Zaragoza radar, lacks the necessary configuration to properly identify supercells using radial wind velocities. They pointed out some problems with the scan strategy, such as the fact that elevations between 1.4° and 7.7°, which are important for identifying the mesocyclone, do not include the base velocity product. Nevertheless, some features can be used as Doppler velocity proxies to assess whether a convective cell is a supercell or not.

Martín et al. (2020) presented a method to identify supercells without using radial velocity data (i.e., non-direct detection of the mesocyclone), based on two-dimensional reflectivity characteristics and severe-weather reports. They proposed that the duration (>60 min exhibiting reflectivity >48 dB*Z*) and the movement of the convective cell (deviant from that of the surrounding radar-observed precipitation structures), together with the observation of at least two of the following radar signatures ((i) hook echo, (ii) BWER at low levels, and (iii) V-notch shape), are sufficient conditions to consider that a convective storm is a supercell with a medium–high confidence. The confirmation is provided by the observation of at least one of the following requirements:

(i) a velocity couplet using Doppler velocity data,
(ii) visual observation of characteristic supercell features,
(iii) an EF3 or stronger tornado (according to the enhanced Fujita scale, Doswell et al. 2009) or
(iv) hail >5 cm in diameter.

The convective cell analyzed here exhibited reflectivity >48 dB*Z* (according to 1-km pseudo-CAPPI, not shown) between 1201 and 1541 UTC (>3.5 h). Moreover, the track was right-deviated from the direction of the pseudo-sounding-calculated mean storm-motion vector (238°), following the direction of the right-moving supercell vector (273°) (see Figs. 1 and 5, and section 3.b). All three reflectivity radar signatures, which are the hook echo, the BWER, and the V-notch, were detected (Fig. 11). Finally, giant hail (⌀ >10 cm) was reported as presented in section 2.f. Therefore, according to Martín et al. (2020), we are confident in inferring that the convective cell was a supercell, although the mesocyclone was not directly detected due to the lack of midlevel Doppler velocity data.

As pointed out by Stough et al. (2017), mesocyclogenesis may be inferred through Doppler velocity interpretation, but also through characteristic reflectivity features such as the BWER or hook echo. However, unlike the mesocyclone, the BWER is not unique to supercells. Still, the development of these reflectivity features in an environment conducive to supercell production signals the presence of strong updrafts and related convective intensification. The lightning hole reinforces this interpretation.

d. Conditions for giant hail

"Giant hail," defined by Knight and Knight (2001) as hail >10 cm in diameter, is a relatively rare phenomenon in the Iberian Peninsula (Farnell et al. 2023). According to Blair et al. (2011), giant hail is almost exclusive to supercells, generally exhibiting cyclonic rotation. Following the findings by Lemon (1978), many giant-hail cases reported by Blair et al. (2011) were also associated with a BWER structure. Indeed, the BWER signature is one of the more significant severe-weather signatures for operational forecasters (Burgess and Lemon 1990). The BWER indicates a wide and strong updraft, which typically contains large amounts of SLW along the outskirts and BWER summit, thereby supporting large-hail growth (Knight and Knight 2005).

The presence of large reflectivities (>50 dB*Z*) in the hail-growth zone (within the –10°C to –30°C layer) indicates the potential for severe hail. This is comparable to training guidelines from the U.S. National Weather Service, which suggest that elevated reflectivity values (≥60 dB*Z*) at or above the –20°C layer indicate an increased hazard of hail (NWS 2006). The presence of Z >60 dB*Z* is almost constant in the Zaragoza radar sequence, and the TOP-60 product showed values above the altitude of the –20°C isotherm (estimated at 7 km MSL) in the 1340, 1410, and 1420 UTC frames (not shown). Donavon and Jungbluth (2007) correlated hail size to a relationship between the environmental melting level and the 50-dBZ reflectivity height (TOP-50). In our case (Fig. 6), the TOP-50 was well above 7 km MSL between 1150 and 1550 UTC (isotherm –20°C estimated at 7 km MSL).

e. TBSS

Blair et al. (2011) reported that the TBSS was present for 20 min in around half of the observed storms bearing giant hail. In the present case study, the TBSS was observed in the radar sequence between 1240 and 1450 UTC (Fig. 10), as a result of the presence of high reflectivity values (>50 dB*Z*) at mid to high levels (TOP-50 was between 10–14 km MSL during this period). Hail observations were reported during this period (Fig. 2).

The TBSS signal is often a sufficient indicator of the occurrence of large hail but is not a necessary radar signature when determining the presence of large hail (NWS 2006). The Meteorological Service of Catalonia studied how this signature could be used to estimate hail size (Rigo and Farnell 2023) and found that it is not always present, even when there are high reflectivity values. Occasionally, nearby thunderstorms can hinder it. Contrarily, there could be some misidentifications of the signature, as it can be confused with electromagnetic interferences (e.g., Altube et al. 2015).

f. Lightning sparkles in the overshooting top

While the bulk of the lightning occurred <12 km MSL, the storm also featured significant activity well above the EL. The LMA system detected high-altitude VHF sources, occurring at 15–16 km MSL above the region of the lightning hole. These distinct VHF sources appear to be discrete, consisting of persistent low-rate sources that lack defined paths. Due to the sporadic nature of these little discharges or sparks, Scholten et al. (2023) designate them as "sparkles." The origin of these phenomena remains unclear. Researchers have linked them to blue corona discharges observed from space (Chanrion et al. 2017; Dimitriadou et al. 2022; Soler et al. 2021). However, sparkles are likely not a singular form of discharge, but compact lightning flashes. MacGorman et al. (2008) and Emersic et al. (2011), among others, pointed to the charge elevated into the overshooting top by the vigorous updraft, causing significant gradients over a short horizontal distance with the opposite polarity of the screening layer, resulting in these small flashes reported in the overshooting tops. However, the purpose of this discussion is not to gain new insights into their origin, but to provide additional evidence supporting their usefulness as a severe-weather pattern. Other LMA networks have reported sparkles in supercell overshooting tops before (Krehbiel et al. 2002; Bruning et al. 2010; Emersic et al. 2011; Calhoun et al. 2013). The present case study relates sparkle periods to a sudden rise in the TOP-50 on the mesocyclone's rear flank region. In line with MacGorman et al. (2017), the largest hail reports (⌀ ≥ 10 cm) occurred while this signature was present, even if some smaller hail can precede the continuum of sparkles. These results provide new evidence of the potential utility of overshooting top sparkles as severe-weather indicators.

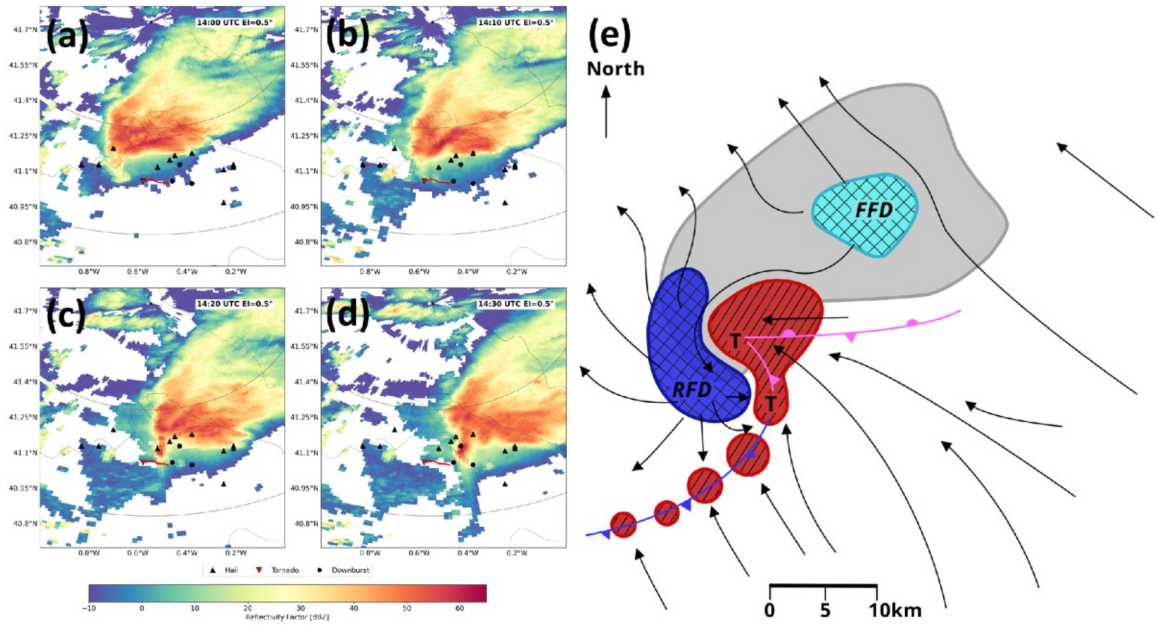

Figure 14: Reflectivity factor (d*BZ*) at 0.5° elevation angle and a) 1400 UTC, b) 1410 UTC, c) 1420 UTC, and d) 1430 UTC, zoomed to the area affected by strong, damaging convective winds, showing hail (black triangles), downburst (black dots) and tornado reports (red triangle and line), and e) schematic representation of classic supercell structure, adapted from Lemon and Doswell (1979), where the rear-flank downdraft (RFD, dark blue), the forward-flank downdraft (FFD, light blue), updrafts (red) and the precipitation region (grey) are shown. T indicates the most suitable location for tornadoes. *Click image to enlarge.*

g. Tornadogenesis and downburst occurrence

By comparing fieldwork results (details in Appendix A) with the radar imagery sequence, it is possible to estimate the time of each strong-convective wind event (with an uncertainty of ±5 min). We estimate the tornado formed at ≈1405 UTC and lasted >10 min. The first downburst occurred also around 1405 UTC, in Area 4 in Fig. A1. Moreover, two downbursts were registered after tornado dissipation, at 1420 UTC (Area 3 in Fig. A1) and around 1430 UTC (Area 5 in Fig. A1). Therefore, surface convective damaging winds were reported after giant-hail observations. De Martin et al. (2025) showed a similar evolution in a tornadic and gigantic hail-producing supercell in northern Italy, where the increasing surface wind gusts were registered while hail size was decreasing in observations.

Prior to tornadogenesis, a BWER was observed, indicating the strength of the updraft. The increase in total-lightning rate also supports this interpretation (Goodman et al. 2005). However, just before tornado formation, total-lightning activity decreased, which may indicate the strengthening of downdrafts (Steiger et al. 2007). This evolution is consistent with tornadogenesis in supercells, where a strong and organized updraft coexists with an intensifying rear-flank downdraft (RFD), potentially leading to tornado formation through the organization of vertical vorticity by transporting angular momentum toward the surface (Lemon and Doswell 1979; Markowski and Richardson 2009). Interestingly, the evolution of total lightning observed here differs from that documented by Krehbiel et al. (2002), who reported an increase in total-lightning activity and the presence of a lightning hole during tornadogenesis and throughout the tornado life cycle. Moreover, the other two downbursts occurred during a period of decreasing total-lightning activity, following a prior increase, consistent with the observations of Goodman et al. (2005) and Steiger et al. (2007), and suggesting a strengthening of downdrafts.

Analyzing the location of each phenomenon relative to the thunderstorm reflectivity shape, it is possible to infer the region of the supercell where each phenomenon took place (Fig. 14). The tornado was formed not exactly under the mesocyclone (according to the hook echo) but 5 km to the south, which means that it was detached from the main mesocyclone (Wurman and Kosiba 2013). It was spawned in the NE quadrant of the rear-flank downdraft, as depicted in Broyles et al. (2022).

Together with tornadogenesis, a downburst took place around 15 km east of the mesocyclone and 8 km north of the rest of the severe-winds reports. The predominant fall direction of uprooted trees was to the southeast (see Appendix A, which lets us infer that it was spawned by the forward-flank downdraft (FFD). Right after the tornado dissipated, the second downburst occurred 5 km to the south of the mesocyclone. According to Fig. 14, this downburst likely was associated with the RFD. Finally, a third RFD-related downburst was observed. Note the alignment of the tornado track with the areas affected by the first and third downbursts.

5. Summary

Forecasters base most of their warning decisions strongly on radar data. Even experienced meteorologists often struggle to consult and integrate various meteorological information during surveillance tasks (warning decision paradigm, Stumpf et al. 2010). Incorporating additional data sources, such as the Lightning Mapping Array (LMA), is likely to be beneficial enough to justify the effort involved. Surveys regarding the use of LMA in the US National Weather Service (NWS) (Darden et al. 2010; Stano et al. 2014) indicate that real-time LMA data significantly improve forecasting and warning-decision making. Total-lightning information provides forecasters with additional confidence in identifying areas where convection is forming or intensifying. Additionally, the real-time availability of these data helps bridge the gap between radar volume scans, especially during rapid storm intensification, and could be explored as a means of gap filling when radar data are unavailable.

LMA data can effectively indicate severe-weather patterns in real-time surveillance, providing valuable insights that complement traditional radar (e.g., storm splitting, BWER, TBSS) and satellite (e.g., overshooting tops, above-anvil cirrus plume and V shape) signatures. Trends in flash rates are widely used operationally to detect thunderstorm intensification through the lightning-jump technique (e.g., Schultz et al. 2009; Chronis et al. 2015; Farnell et al. 2017), based on a statistically significant increase in lightning activity within a brief timeframe. Furthermore, total-lightning utility may be extended beyond signaling updraft intensification to infer the development and strengthening of the midlevel rotation in environments supporting supercells. LMA-derived signatures, such as lightning holes and sparkles in overshooting tops, show strong potential for operational weather surveillance applications. These severe-weather signatures can visually complement the automated lightning "jump" as early warning indicators to trained forecasters.

Although this case study may appear to be an unusual and extremely severe weather event, incidents of giant hail are becoming more frequent in the Mediterranean region (e.g. Farnell et al. 2023; Montopoli et al. 2021). In light of this trend, meteorological services require ever-increasing preparedness in monitoring capabilities and improvement of the accuracy of early warning systems.

ACKNOWLEDGMENTS

The authors are thankful to Sergi Pujolar, Marta Balagué, Patri Altube and Helen San Segundo, all from the Meteorological Service of Catalonia, for their contributions. The authors are grateful to Consorcio de Compensación de Seguros (CCS) for providing data from the damaging winds fieldwork and to Agencia Estatal de Meteorología, and Ministerio para la Transición Ecológica y el Reto Demográfico for providing Zaragoza radar data. This work was supported by research grants PID2022-136348NB-C32, PID2019-109269RB-C42, EQC2021-450 006957-P, funded by MICIU/AEI/10.13039/501100011033 and by European Union Next Generation EU/RRP. This material is based upon work supported by the NSF National Center for Atmospheric Research, which is a major facility sponsored by the U.S. National Science Foundation under Cooperative Agreement No. 1852977.

APPENDIX A: FIELDWORK

After the strong convective wind event, a damage survey was performed to analyze which meteorological phenomenon occurred (i.e., tornado or downburst), to assess the size and characteristics of the affected area, and to estimate the wind intensity. The fieldwork was conducted on 12, 15, 22, and 28 July, 2023, following the methodology presented in Rodríguez et al. (2020). Data collected included 582 damaged elements (trees and man-made structures) with respective georeferenced images. Moreover, the direction of fall for uprooted trees and windborne debris was reported to analyze the damage pattern. These patterns present convergence and rotation in the case of tornadoes, with divergent swaths observed in the case of downbursts (Bech et al. 2009, 2011).

The fieldwork was conducted in an area which extended 20 km west–east and 12 km north–south, ≈70 km southeast of Zaragoza. The affected area is characterized by the Martín River Valley, which extends southwest to northeast in the western part of the region. The valley is surrounded by the Sierra de Arcos mountain range, with peaks reaching 400 m above the valley (i.e., 850 meters MSL).

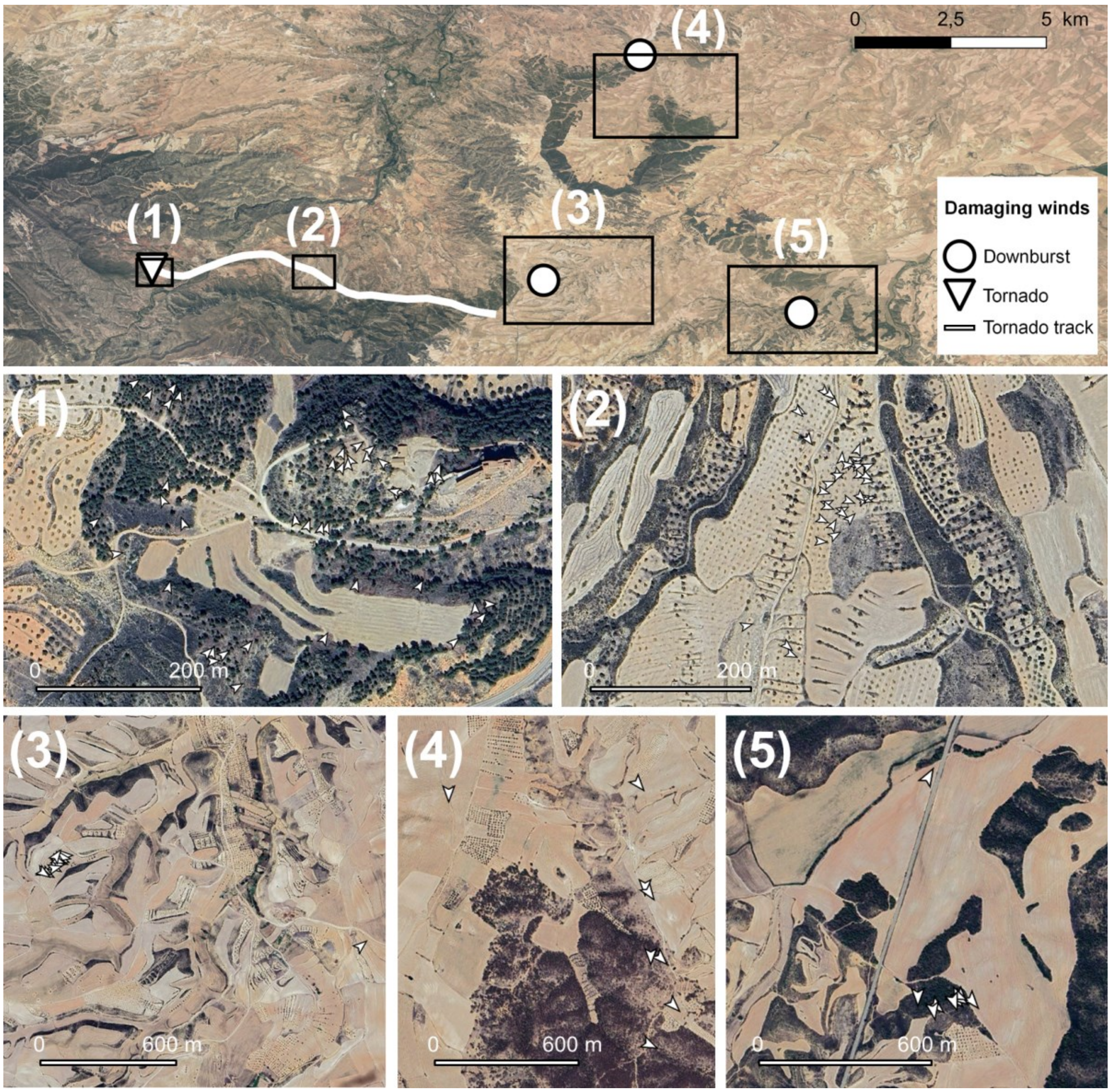

Figure A1: In the main map, tornado (triangle) and downbursts (circle) reports are shown, together with the tornado track. The white line represents the tornado track. Black squares indicate the zoomed areas shown in (1), (2), (3), (4), and (5) subplots, where white arrows represent the direction of the fallen trees. *Click image to enlarge.*

The central and eastern regions are flatter with some hills that generally do not rise above 600 meters MSL. This area is dominated by open fields with a low density of possibly damaged elements, which can hinder data collection tasks.

A 19.5-km-long damage path, oriented west to east, was identified (sectors 1 to 5, except 4, in Fig. A1) along with a secondary damaged area located 8 km to the north (sector 4 in Fig. A1). The fallen trees presented rotation signs (Fig. A1, Area 1) in the western region of the most extensive damage swath, along with a convergence pattern (Fig. A1, Area 2). Most uprooted trees fell to the north and east, whereas the strong convective wind damage swath was oriented west to east, coinciding with the convective cell track. However, some trees from the left sector of the damaged swath were uprooted to the southeast or even southwest. This indicates the passage of a tornado in this area. On the other hand, in the eastern half of the primary damage path, the fallen trees showed a diverging pattern.

Specifically, trees in the right sector were uprooted toward the southeast and south, while those in the left sector fell to the northeast. Furthermore, two divergence centers were identified with prevailing directions from the first and second quadrants, from which it can be inferred the occurrence of two downbursts (Fig. A1, Areas 3 and 5). Finally, uprooted trees and wind-borne debris from the secondary damaged area located to the north also presented a diverging pattern, associated with another downburst. In this case, though, trees fell to the south (Fig. A1, Area 4). Therefore, three downbursts were detected.

The tornado track was channeled by the river valley and followed the northern Sierra de Arcos mountainside. The damage swath was estimated to be ≈9.6 km long, and 950 m in maximum width. The first downburst (the northernmost), which occurred along with the tornado, affected an area 2.5 km long and 1700 m wide. The second one, located right to the east of the tornado track, caused damage in a zone 6.2 km long and 2600 m wide. The area affected by the eastern downburst measured 5.0 km long and 3800 m wide (Table 1).

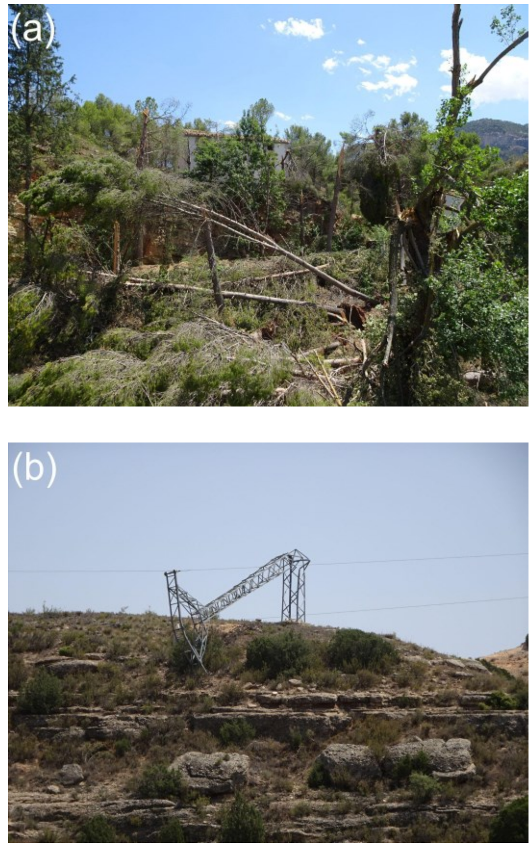

Figure A2: a) Several trees damaged by the tornado, and b) an electricity tower collapsed by the first registered downburst. Author: Salvador Castán. Credit: CCS. *Click images to enlarge.*

Along the tornado damage path, hundreds of pines and poplar trees were uprooted and snapped (Fig. A2a), whereas some of them presented most of their branches broken. Close to the Martín River, areas were found where nearly all trees were affected. Damage to buildings was also observed, such as the partial destruction of brick masonry free-standing walls and the loss of >50% of tiles from roofs. According to the International Fujita scale (ESSL 2023), the tornado should be rated as IF1.5 (i.e., 50 m s^{-1}). Similar damage was reported for downbursts, although all three also produced the collapse of electricity towers (Fig. A2b), providing a higher rating (IF2; 60 m s^{-1}).

APPENDIX B: LMA NETWORK PERFORMANCE

LMA stations record the peak received power of each located event; processed data includes an estimation of the total peak power radiated by the sources (Thomas et al. 2001). The minimal source power detected by a network can be a metric for detection efficiency (Thomas et al., 2004). Tomas et al. (2001) showed that peak power from lightning varies from their minimum network sensitivity of 1 W (0 dB*W*) to kilowatt power levels. Chmielewski and Bruning (2016) characterized the LMA network performance as a function of the distribution of source powers, presenting a P-1 distribution starting at –10 dBW and peaking just above 0 dB*W*. Similarly, we have calculated this metric for the day of interest. Figure B1 shows the storm of interest starting in a low-sensitivity area. Sensitivity improves during the trajectory of the storm, while approaching the center of the LMA.

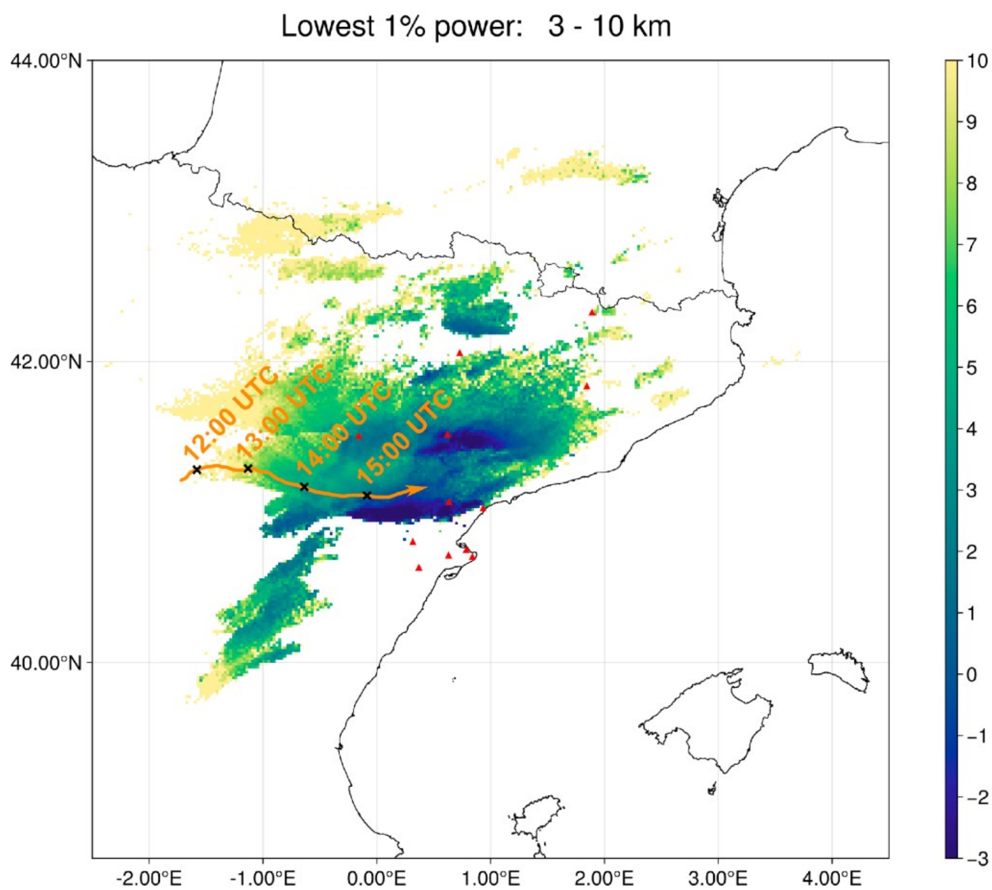

Figure B1: Characterization of the LMA network performance on the day of study (6 July 2023) as function of the distribution of source power (dB*W*). The arrow with time stamps corresponds to the supercell trajectory.

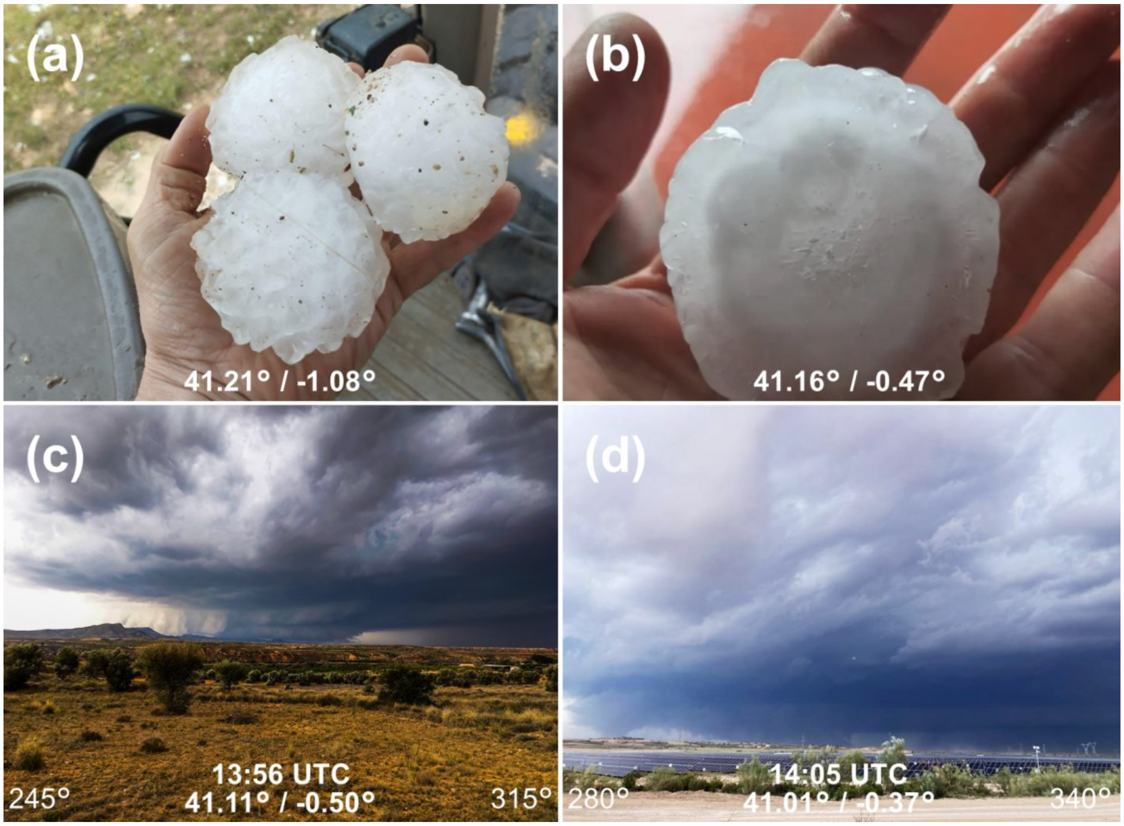

Figure C1: a) Large hail in Herrera de los Navarros (source: Enrique Felices / heraldo.es) and b) in Urrea de Gaén (source: heraldo.es); c) overview of the storm's base structure from Albalate del Arzobispo (source: Marc Sanz / @Stormyalert); and d) general view of the storm base with the tornadic condensation funnel on the left side (retrieved from the map viewer of the "Base de Datos de Tiempo Severo: granizo (2000–2024) y tornados (2011–2024)", from @Supercelulas, available at arcg.is/1bPe9n). In all images, the time they were taken is shown, and in (c) and (d), the directions of the left and right edges (in degrees) are also indicated. *Click image to enlarge.*

APPENDIX C: PHOTOGRAPHS FROM THE SEVERE-WEATHER OUTBREAK

Several users from social media shared images of the thunderstorm, from gigantic hailstones to the tornado, together with the damage caused in the area. Figure C1a exhibits large hailstones reported around 13:00 UTC in Herrera de los Navarros, the first municipality with a hail maximum diameter >10 cm (Table 1).

In the map shown in Fig. 2, it corresponds to report 1. Figure C1b shows large hail in Urrea de Gaén around 1400 UTC. According to the severe-weather databases consulted, the maximum observed diameter in this municipality was 6 cm. This picture corresponds to the hail reports located just west of report 6 in Fig. 2.

The third photo (Fig. C1c) was taken at 1356 UTC (i.e., 9 min before the tornado and the first downburst) in Albalate del Arzobispo (just 8 km northeast of the tornado touchdown location, report 5 in Fig. 2). Here, a general view of the forward-flank cumulonimbus base is shown, looking westward prior to the passage of the storm. A characteristic feature commonly observed in supercells can be identified in the center of the image: the wall cloud. Precipitation is present on the right side, whereas the cloud base on the left side is precipitation-free. These observations are consistent with the classical supercell model. Finally, in Fig. C1d, the wall cloud can also be seen in the central part of the image, while the tornadic funnel is visible on the left side. This photo was taken at 1405 UTC from a location ≈18.5 km east-southeast of the tornadogenesis site (i.e., the photo is oriented toward the NW).

REFERENCES

Adler, R. F. and R. A. Mack, 1986: Thunderstorm cloud top dynamics as inferred from satellite observations and a cloud top parcel model. *J. Atmos. Sci.*, **43**, 1945–1960.

Agroseguro, 2023: La superficie siniestrada por las fuertes tormentas de pedrisco registradas el pasado jueves y viernes se eleva hasta las 30.000 hectáreas aseguradas. Agroseguro, Madrid, Spain. [Available online at https://agroseguro.es/la-superficie-siniestrada-por-las-fuertes-tormentas-de-pedrisco-registradas-el-pasado-jueves-y-viernes-se-eleva-hasta-las-30-000-hectareas-aseguradas/]

Altube, P., J. Bech, O. Argemí, and T. Rigo, 2015: Quality control of antenna alignment and receiver calibration using the sun: Adaptation to midrange weather radar observations at low elevation angles. *J. Atmos. Ocean. Technol*., **32**, 927–942.

Aran, M., J. C. Pena, M. Torà, 2011: Atmospheric circulation patterns associated with hail events in Lleida (Catalonia). *Atmos. Res*., **100**, 428–438.

Bech, J., M. Gayà, M. Aran, F. Figuerola, J. Amaro and J. Arús, 2009: Tornado damage analysis of a forest area using site survey observations, radar data and a simple analytical vortex model. *Atmos. Res.*, **93**, 118–130.

Bech, J., N. Pineda, T. Rigo, M. Aran, J. Amaro, M. Gayà, J. Arús, J. Montanyà and O. van der Velde, 2011: A Mediterranean nocturnal heavy rainfall and tornadic event. Part I: Overview, damage survey and radar analysis. *Atmos. Res.*, **100**, 621–637.

Bedka, K., 2011: Overshooting cloud top detections using MSG SEVIRI infrared brightness temperatures and their relationship to severe weather over Europe. *Atmos. Res.*, **99**, 175–189.

——, J. Brunner, R. Dworak, W. Feltz, J. Otkin and T. Greenwald, 2010: Objective satellite-based detection of overshooting tops using infrared window channel brightness temperature gradients. *J. Appl. Meteor. Climatol.* **49**, 181–202.

——, E. M. Murillo, C. R. Homeyer, B. Scarino, and H. Mersiovsky, 2018: The above-anvil cirrus plume: An important severe weather indicator in visible and infrared satellite imagery. *Wea. Forecasting,* **33**, 1159–1181.

Blair, S. F., D. R. Deroche, J. M. Boustead, J. W. Leighton, B. L. Barjenbruch, and W. P. Gargan, 2011: A radar-based assessment of the detectability of giant hail. *Electronic J. Severe Storms Meteor.,* **6** (7), 1–30.

——, and Coauthors, 2017. High-resolution hail observations: Implications for NWS Warning Operations. *Wea. Forecasting,* **32**, 1101–1119.

Bruning, E. C., and D. R. MacGorman. Theory and observations of controls on lightning flash size spectra. *J. Atmos. Sci.*, **70**, 4012–4029.

——, W. D. Rust, D. R. MacGorman, M. I. Biggerstaff, and T. J. Schuur, 2010: Formation of charge structures in a supercell. *Mon. Wea. Rev.,* **138**, 3740–3761.

Bunkers, M. J., B. A. Klimowski, J. W. Zeitler, R. L. Thompson, and M. L. Weisman, 2000: Predicting supercell motion using a new hodograph technique. *Wea. Forecasting,* **15**, 61–79.

Burgess, D. W., and L. R. Lemon, 1990: Severe thunderstorm detection by radar. *Radar in Meteorology,* D. Atlas, Ed., Amer. Meteor. Soc., 619–647.

Calhoun, K. M., D. R. MacGorman, C. L. Ziegler and M. I. Biggerstaff, 2013: Evolution of lightning activity and storm charge relative to dual-Doppler analysis of a high-precipitation supercell storm. *Mon. Wea. Rev.*, **141**, 2199–2223.

——, E. R. Mansell, D. R., MacGorman, and D. C. Dowell, 2014: Numerical simulations of lightning and storm charge of the 29–30 May 2004 Geary, Oklahoma, supercell thunderstorm using EnKF mobile radar data assimilation. *Mon. Wea. Rev.*, **142**, 3977–3997.

Calvo-Sancho, C., and Y. Martín, 2020: The influence of synoptic weather patterns in supercell formation in Spain. Proc., *EGU General Assembly 2020*, EGU2020–40.

——, J. Díaz-Fernández, Y. Martín, P. Bolgiani, M. Sastre, J. J. González-Alemán, D. Santos-Muñoz, J. I. Farrán and M. L. Martín, 2022: Supercell convective environments in Spain based on ERA5: Hail and non-hail differences. *Wea. Climate Dynam.,* **3**, 1021–1036.

Chanrion, O., T. Neubert, A. Mogensen, Y. Yair, M. Stendel, R. Singh, and D. Singh, 2017: Profuse activity of blue electrical discharges at the tops of thunderstorms. *Geophys. Res. Lett.,* **44**, 496–503.

Chmielewski, V. C., and E. C. Bruning, 2016: Lightning mapping array flash detection performance with variable receiver thresholds. *J. Geophys. Res. Atmos.*, **121**, 8600–8614.

——, ——, and B. C. Ancell, 2018: Variations of thunderstorm charge structures in West Texas on 4 June 2012. *J. Geophys. Res. Atmos.*, **123**, 9502–9523.

——., D. R. MacGorman, C. L. Ziegler, E. DiGangi, D. Betten, and M. Biggerstaff, (2020). Microphysical and transportive contributions to normal and anomalous polarity subregions in the 29–30 May 2012 Kingfisher storm. *J. Geophys, Res. Atmos.*, **125**, e2020JD032384.

Chronis, T., L. D. Carey, C. J. Schultz, E. V. Schultz, K. M. Calhoun, and S. J. Goodman, 2015: Exploring lightning jump characteristics. *Wea. Forecasting*, **30**, 23–37.

Craven, J. P., D. Myrick, J. J. Brost, B. M. Rasch, M. Singer, P. M. Iñiguez, and T. I. Alcott, 2015: Culture change: Evolution of the forecast process. Proc., *27th Conf. on Weather Analysis and Forecasting/23rd Conf. on Numerical Weather Prediction,* Chicago, IL, Amer. Meteor. Soc., 7B.6.

Darden, C. B., D. J. Nadler, B. C. Carcione, R. J. Blakeslee, G. T. Stano, and D. E. Buechler, 2010: Utilizing total lightning information to diagnose convective trends, *Bull. Amer. Meteor. Soc.*, **91**, 167–176.

Davies-Jones, R., 2015: A review of supercell and tornado dynamics. *Atmos. Res.,* **158**, 274–291.

De Martin, F., F. Pavan, N. Carlon, G. Cioni, C. Rozoff, V. Poli, S. Carpentari, and M. M. Miglietta, 2025: A significant tornado event near a dryline bulge in northern Italy. *Wea. Forecasting*, **40**, 2293–2315.

Deierling, W., W. A. Petersen, J. Latham, S. Ellis, and H. J. Christian, 2008: The relationship between lightning activity and ice fluxes in thunderstorms. *J. Geophys. Res. Atmos.,* **113**, D15210.

del Moral, A., T. M. Weckwerth, T. Rigo, M. M. Bell, and M. C. Llasat, 2020: C-band dual-Doppler retrievals in complex terrain: Improving the knowledge of severe storm dynamics in Catalonia. *Remote Sens.*, **12** 18, 2930.

Dimitriadou, K., O. Chanrion, T. Neubert, A. Protat, V. Louf, M. Heumesser, L. Husbjerg, C. Köhn, N. Østgaard, and V. Reglero, 2022: Analysis of blue corona discharges at the top of tropical thunderstorm clouds in different phases of convection. *Geophys. Res. Lett.,* **49**, e2021GL095879.

Donavon, R. A., and K. A. Jungbluth, 2007: Evaluation of a technique for radar identification of large hail across the Upper Midwest and Central Plains of the United States. *Wea. Forecasting*, **22**, 244–254.

Doswell, C. A. III, H. E. Brooks, and N. Dotzek, 2009: On the implementation of the enhanced Fujita scale in the USA. *Atmos. Res.*, **93**, 554–563.

Dotzek, N., P. Groenemeijer, B. Feuerstein, and A.M. Holzer, 2009: Overview of ESSL's severe convective storms research using the European Severe Weather Database ESWD. *Atmos. Res.*, **93**, 575–586.

Edwards, R., and R. L. Thompson, 1998: Nationwide comparisons of hail size with WSR-88D vertically integrated liquid water and derived thermodynamic sounding data. *Wea. Forecasting*, **13**, 277–285.

Emersic, C., P. L. Heinselman, D. R. MacGorman, and E. C. Bruning, 2011: Lightning activity in a hail-producing storm observed with phased-array radar. *Mon. Wea. Rev.*, **139**, 1809–1825.

European Severe Storms Laboratory (ESSL), 2023: The International Fujita (IF) scale for tornado and wind damage assessments. [Available online at https://www.essl.org/cms/wp-content/uploads/IF-scale_v1.0d.pdf.]

Farnell, C., T. Rigo, and N. Pineda, 2017: Lightning jump as a nowcast predictor: Application to severe weather events in Catalonia. *Atmos. Res.*, **183**, 130–141.

——, E. Batalla, T. Rigo, N. Pineda, X. Sole, J. Mercader, and J. Martin-Vide, 2023: Reanalysis of giant hail event in Catalonia (NE of the Iberian Peninsula). *Atmos. Res.*, **296**, 107051.

Fujita, T. T., 1978: Manual of downburst identification for project NIMROD, SMRP 156, University of Chicago, 104 pp.

García-Ortega, E., L. López, and J. L. Sánchez, 2011: Atmospheric patterns associated with hailstorm days in the Ebro Valley, Spain. *Atmos. Res.*, **100**, 401–427.

Gatlin, P. N., and S. J. Goodman, 2010: A total lightning trending algorithm to identify severe thunderstorms. *J. Atmos. Oceanic Technol.*, **27**, 3–22.

Goodman, S. J., and Coauthors, 2005: The North Alabama Lightning Mapping Array: Recent severe storm observations and future prospects. *Atmos. Res.*, **76**, 423–437.

Gutiérrez-Rubio, D., J. Riesco, and S. Ponce, 2015: SINOBAS, a tool for collaborative mapping applied to observation of "singular" weather phenomena. Proc., *15th EMS Ann. Meeting and 12th European Conf. on Applications of Meteorology (ECAM),* Sofia, Bulgaria, EMS2015-413.

Hersbach, H., et al. 2020: The ERA5 global reanalysis, *Quart. J. Roy. Meteorol. Soc.*, **146**, 1999–2049.

Heymsfield, G. M., and R. H. Blackmer Jr, 1988: Satellite-observed characteristics of Midwest severe thunderstorm anvils. *Mon. Wea. Rev.*, **116**, 2200–2224.

Jayaratne, R., and C. Saunders, 2014: Wet hail and thunderstorm electrification. Proc., 15th *International Conf. on Atmospheric Electricity,* Norman, OK, , 6 pp.

Klemp, J. B., and R. B. Wilhelmson, 1978: Simulations of right- and left-moving storms produced through storm splitting. *J. Atmos. Sci.*, **35**, 1097–1110.

Knight, C. A., and N. C. Knight, 2001: Hailstorms. *Severe Convective Storms, Meteor. Monogr.*, No. 50, Amer. Meteor. Soc., 223–254..

——, and ——, 2005: Very large hailstones from Aurora, Nebraska. *Bull. Amer. Meteor. Soc.*, **86**, 1773–1782.

Koshak, W. J., and Coauthors, 2004: North Alabama Lightning Mapping Array (LMA): VHF source retrieval algorithm and error analyses, *J. Atmos. Oceanic Technol.*, **21**, 543–558.

Krehbiel, P., T. Hamlin, Y. Zhang, J. Harlin, R. Thomas, and W. Rison, 2002: Three-dimensional total lightning observations with the lightning mapping array. Preprints, *International Lightning Detection Conf.*, Tucson, AZ, 6 pp.

Kumjian, M. R., and A. V. Ryzhkov, 2008: Polarimetric signatures in supercell thunderstorms. *J. Appl. Meteor. Climatol.*, **47**, 1940–1961.

——, K.. Lombardo, and S. Loeffler, 2021: The evolution of hail production in simulated supercell storms. *J. Atmos. Sci.*, **78**, 3417–3440.

Lane, T. P., R. D. Sharman, T. L. Clark, and H.-M. Hsu, 2003: An investigation of turbulence generation mechanisms above deep convection. *J. Atmos. Sci.*, **60**, 1297–1321.

Lang, T. J., S. A. Rutledge, and K. C. Wiens, 2004: Origins of positive cloud-to-ground lightning flashes in the stratiform region of a mesoscale convective system. *Geophys. Res. Lett.*, **31**, L10105.

Lemon, L. R., 1977: New severe thunderstorm radar identification techniques and warning criteria: A preliminary report. NOAA Tech. Memo. NWS NSSFC-1, 60 pp. [NTIS PB-273049.]

——, 1978: On the use of storm structure for hail identification. Preprints, *18th Conf. on Radar Meteorology*, Boston, MA, Amer. Meteor. Soc., 203–206.

——, and C. A. Doswell III, 1979: Severe thunderstorm evolution and mesocyclone structure as related to tornadogenesis. *Mon. Wea. Rev.*, **107**, 1184–1197.

Lindley, T. T., and L. R. Lemon, 2007: Preliminary observations of weak three-body scatter spikes associated with low-end severe hail. *Electronic J. Severe Storms Meteor.*, **2**, 1–15.

Lyons, W. A., T. E. Nelson, R. A. Armstrong, V. P. Pasko, and M. A. Stanley, 2003: Upward electrical discharges from thunderstorm tops. *Bull. Amer. Meteor. Soc.*, **84**, 445–454.

MacGorman, D. R., W. D. Rust, P., Krehbiel, W. Rison, E. Bruning, and K. Wiens, 2005: The electrical structure of two supercell storms during STEPS. *Mon. Wea. Rev.*, **133**, 2583–2607.

——, and Coauthors, 2008. TELEX The Thunderstorm Electrification and Lightning Experiment. *Bull. Amer. Meteor. Soc.*, 89, 997–1013.

——, M. S. Elliott, and E. DiGangi, 2017: Electrical discharges in the overshooting tops of thunderstorms. *J. Geophys. Res. Atmos.*, **122**, 2929–2957.

Mazur, V., 2002: Physical processes during development of lightning flashes. *Comptes Rendus Physique*, **3**, 1393–1409.

McCaul, E. W. Jr., J. Bailey, J. Hall, S. J. Goodman, R. J. Blakeslee, and D. E. Buechler, 2005: A flash clustering algorithm for North Alabama Lightning Mapping Array data. Preprints, *Conf. on Meteorological Applications of Lightning Data,* San Diego, CA, Amer. Meteor. Soc., 5.2.

——, S. J. Goodman, K. M. LaCasse, and D. J. Cecil, 2009: Forecasting lightning threat using cloud-resolving model simulations. *Wea. Forecasting*, **24**, 709–729.

McKinney, C. M., Carey, L. D., & Patrick, G. R. (2009). Total lightning observations of supercells over north central Texas. *Electronic J. Severe Storms Meteor.*, **4** (2), 1–25.

Markowski P. M., and Y. P. Richardson, 2009: Tornadogenesis: Our current understanding, forecasting considerations, and questions to guide future research. *Atmos. Res.*, **93**, 3–10.

Martín Y., M. Cívica and E. Pham, 2020: Constructing a supercell database in Spain using publicly available two-dimensional radar images and citizen science. *Annals Amer. Assoc. Geogr.*, **111**, 1346–1366.

Mecikalski, R. M., and L. D. Carey, 2018: Radar reflectivity and altitude distributions of lightning flashes as a function of three main storm types. *J. Geophys. Res. Atmos.*, **123**, 12 814–12 828.

Metzger, E., and W. A. Nuss, 2013: The relationship between total cloud lightning behavior and radar-derived thunderstorm structure. *Wea. Forecasting*, **28**, 237–253.

Montopoli, M., E. Picciotti, L. Baldini, S. Di Fabio, F. S. Marzano, and G. Vulpiani, 2021: Gazing inside a giant-hail-bearing Mediterranean supercell by dual-polarization Doppler weather radar, *Atmos. Res.*, **264**, 105852.

Murphy, M. J., and N. W. Demetriades, 2005: An analysis of lightning holes in a DFW supercell storm using total lightning and radar information. Preprints, *Conf. on Meteorological Applications of Lightning Data*, San Diego, CA, Amer. Meteor. Soc., 2.3.

Negri, A. J., and R. F. Adler, 1981: Relation of satellite-based thunderstorm intensity to radar-estimated rainfall. *J. Appl. Meteor. Climatol.*, **20**, 288–300.

Nixon, C. J., and J. T. Allen, 2022: Distinguishing between hodographs of severe hail and tornadoes. *Wea. Forecasting,* **37**, 1761–1782.

NWS Warning Decision Training Branch, 2006: Three body scatter spike. Advanced Warning Operations Course: Storm Interrogation. [Available online at: http://ejssm.org/ojs/public/vol2-3/ICSvr3-V-A_TBSS.pdf.]

de Pablo Dávila, F., L. J. Rivas Soriano, C. Jiménez Alonso, M. Mora García, and J. Riesco Martín, 2021: Synoptic patterns of severe hailstorm events in Spain. *Atmos. Res.*, **250**, 105397.

Payne, C. D., T. J. Schuur, D. R. MacGorman, M. I., Biggerstaff, K. M. Kuhlman, and W. D. Rust, 2010: Polarimetric and electrical characteristics of a lightning ring in a supercell storm. *Mon. Wea. Rev.*, **138**, 2405–2425.

Punge, H. J., and M. Kunz, 2016: Hail observations and hailstorm characteristics in Europe: A review. *Atmos. Res.*, **176**, 159–184.

Quirantes, J. A., J. Riesco, and J. A. Nuñez. 2014: Caracterısticas basicas de las supercelulas en España [EN: Basic characteristics of supercells in Spain]. Accessed March 27, 2025. [Available online at https://www.aemet.es/documentos/es/conocermas/recursos_en_linea/publicaciones_y_estudios/publicaciones/Caracteristicas_supercelulas/Caracteristicas_supercelulas.pdf.]

Rigo, T., and C. Farnell, 2023: Preliminary analysis of early identification of three-body scatter spike signature in hailstorms in Catalonia. *Atmosphere,* **14**, 269.

——, and ——, 2024: A comparison between radar variables and hail pads for a twenty-year period. *Climate*, **12**, 158.

Rison, W., R. J. Thomas, P. R. Krehbiel, T. Hamlin and J., Harlin, 1999: A GPS-based three-dimensional lightning mapping system: Initial observations in central New Mexico. *Geophys. Res. Lett*., **26**, 3573–3576.

Rodríguez, O., and J. Bech, 2021. Tornadic environments in the Iberian Peninsula and the Balearic Islands based on ERA5 reanalysis. *Int. J. Climatol.*, **41**, E1959–E1979.

——, and M. Lemus-Canovas, 2023. Synoptic patterns triggering tornadic storms on the Iberian Peninsula and the Balearic Islands. *Atmos. Res.*, **285**, 106634.

——, J., Bech, J.D. Soriano, D. Gutiérrez, S. Castán, 2020: A methodology to conduct wind damage field surveys for high-impact weather events of convective origin. *Nat. Haz. Earth Sys. Sci.*, **20**, 1513–1531.

Salvador, A., N. Pineda, J. Montanyà, J.A. López, and G. Solà, 2021: Thunderstorm charge structures favouring cloud-to-ground lightning. *Atmos. Res.*, **257**, 105577.

Saunders, C. P. R., and I. M. Brooks, 1992: The effects of high liquid water content on thunderstorm charging. *J. Geophys. Res. Atmos.*, **97**, 14671–14676.

Scholten, O., B. M. Hare, J. Dwyer, N. Liu, C. Sterpka, J. Assink, H. Leijnse, and S. ter Veen, 2023: Small-scale discharges observed near the top of a thunderstorm. *Geophys. Res. Lett.*, **50**, e2022GL101304.

Schultz, C. J., W. A. Petersen, and L. D. Carey, 2009: Preliminary development and evaluation of lightning jump algorithms for the real-time detection of severe weather. *J. Appl. Meteor. Climatol.*, **48**, 2543–2563.

——, ——, and ——, 2011: Lightning and severe weather: A comparison between total and cloud-to-ground lightning trends. *Wea. Forecasting*, **26**, 744–755.

——, L. D. Carey, E. V. Schultz, and R. J. Blakeslee, 2017: kinematic and microphysical significance of lightning jumps versus nonjump increases in total flash rate. *Wea. Forecasting*, **32**, 275–288,

Setvák, M., Z.,Charvát, M. Valachová, and K. Bedka, 2012: Blended "sandwich" image products in nowcasting. Proc., *2012 EUMETSAT Meteorological Satellite Conf.*, Sopot, Poland, EUMETSAT, 61.

Sharp, D. W., 2005: Operational applications of lightning data at WFO Melbourne, FL: A 15-year retrospective. Preprints, *Conf. on Meteorological Applications of Lightning Data*, San Diego, CA, Amer. Meteor. Soc., 1.1.

Soler, S., and Coauthors, 2020: Blue optical observations of narrow bipolar events by ASIM suggest corona streamer activity in thunderstorms. *J. Geophys. Res. Atmospheres,* **125**, e2020JD032708.

Stano, G. T., C. J. Schultz, L. D. Carey, D. R. MacGorman, and K. M. Calhoun, 2014: Total lightning observations and tools for the 20 May 2013 Moore, Oklahoma, tornadic supercell. *J. Oper. Meteor.*, **2**, 71–88.

Steiger, S. M., R. E. Orville, and L. D. Carey, 2007: Total lightning signatures of thunderstorm intensity over north Texas. Part II: Mesoscale convective systems. *Mon. Wea. Rev*., **135**, 3303–3324.

Stough, S. M., L. D. Carey, C. J. Schultz and P. M. Bitzer, 2017: Investigating the relationship between lightning and mesocyclonic rotation in supercell thunderstorms. *Wea. Forecasting*, **32**, 2237–2259.

Stumpf, G. J., B. C. Baranowski, D. M. Kingfield, K. M. Kuhlman, K. L. Manross, C. W. Siewert, T. M. Smith, and S. Stough, 2010: Real-time severe convective weather warning exercises at the 2010 Experimental Warning Program (EWP2010). *Preprints, 25th Conf. on Severe Local Storms,* Denver, CO, Amer. Meteor. Soc., 7B.2.

Takahashi, T., 1978: Riming electrification as a charge generation mechanism in thunderstorms. *J. Atmos. Sci.*, **35**, 1536–1548.

Taszarek, M., J. T. Allen, T. Púčik, K. A. Hoogewind, and H. E. Brooks, 2020: Severe convective storms across Europe and the United States. Part II: ERA5 environments associated with lightning, large hail, severe wind, and tornadoes. *J. Climate*, **33**, 10263–10286.

Thomas, R. J., P. R. Krehbiel, W. Rison, T. Hamlin, J. Harlin, and D. Shown, 2001: VHF source powers radiated by lightning, *Geophys. Res. Lett.*, **28**, 143–146.

——, P. R. Krehbiel, W. Rison, S. J. Hunyady, W. P. Winn, T. Hamlin, and J. Harlin, 2004. Accuracy of the lightning mapping array. *J. Geophys. Res.* 109, D14207.

Thompson, R. L., R. Edwards, J. A. Hart, K. L. Elmore, and P. M. Markowski, 2003: Close proximity soundings within supercell environments obtained from the Rapid Update Cycle. *Wea. Forecasting*, **18**, 1243–1261.

ThunderR, accessed 2024: ERA5 sigma levels browser Europe. 2024. [Available online at: http://www.rawinsonde.com/ERA5_Europe/]

Van Den Broeke, M. S. and E. R. Green, 2024: Temporal associations between polarimetric updraft proxies and signatures of inflow and hail in supercells. *Remote Sens.*, **16**, 4314.

van der Velde, O.A., 2024: Visualization and analysis of 3D lightning mapping array data. Proc., Juliacon, Eindhoven, Netherlands. https://pretalx.com/juliacon2024/talk/review/RPVBHWUTB3B8KGPPESTVGWFRGM7B3XRX

Williams, E., V. Mushtak, D. Rosenfeld, S. Goodman, and D. Boccippio, 2005: Thermodynamic conditions favorable to superlative thunderstorm updraft, mixed phase microphysics and lightning flash rate. *Atmos. Res.*, **76**, 288–306.

Wiens, K. C., S. A. Rutledge, and S. A. Tessendorf, 2005: The 29 June 2000 supercell observed during STEPS. Part II: Lightning and charge structure. *J. Atmos. Sci.*, **62**, 4151–4177.

Wurman, J., and K. Kosiba, 2013: Finescale radar observations of tornado and mesocyclone structures. *Wea. Forecasting*, **28**, 1157–1174.

Zhang, Y., Q. Meng, P. R. Krehbiel, X. Liu, and X. Zhou, 2004: Spatial and temporal characteristics of VHF radiation source produced by lightning in supercell thunderstorms. *Chin. Sci., Bull.*, **49**, 624–631.

Ziegler, C. L., E. R. Mansell, K. M. Calhoun, and D. R. MacGorman, 2014: Impact of kinematics, microphysics, and electrification on the formation of lightning-weak holes in a simulated supercell storm. Proc., 15th *International Conf. on Atmospheric Electricity*, Norman, OK, 16 pp..

Zrnić, D. S., 1987: Three-body scattering produces precipitation signature of special diagnostic value. *Radio Sci.*, **22**, 76–86.

——, G. Zhang, V. Melnikov, and J. Andric, 2010. Three-body scattering and hail size. *J. Appl. Meteor. Climatol.*, **49**, 687–700.

REVIEWER COMMENTS

[Authors' responses in *blue italics.*]

REVIEWER A (Vanna C. Chmielewski):

Initial Review:

Recommendation: Accept with major revisions.

Overall Comment: The authors provide a detailed case study of a (presumed) supercell which produced severe weather in the Iberian Peninsula over multiple hours. Their case study includes a description of the background environment and synoptic conditions, the presentation of lightning features captured with the Ebro Lightning Mapping Array, and radar reflectivity characteristics, with a focus on the timing of each feature's evolution as potential early warning signs of its severity. I appreciate their thorough discussion of individual components.

My overall struggle with this paper was that it in essence seemed to just present indicators of an intense updraft, but did not put the useful effort into either: 1) methodically aligning the components discussed, or 2) include more detailed comparison (with more demonstration) of the individual components to prior cases. Efforts in some combination of (1) and/or (2) would make this a much more impactful study. Some specific suggestions are below.

We greatly appreciate your helpful and insightful review, which we believe has significantly enhanced the first manuscript. In light of the comments, the study has undergone a major overhaul with many changes, including section rearrangements, figure and reference additions, and many other minor changes.

Following this first general comment, we have changed the approach of the results presented by analyzing the evolution of the storm instead of focusing only on severe-weather signatures. The new analysis is now based on four periods into which we have divided the episode. Besides, ancient Fig. 14 has been improved to summarize the episode (now Fig. 6), and a new figure (Fig. 7) has been added to show the whole evolution of LMA data.

Major Comments: Influence of storm track on analysis: The storm of interest appears to have started ≈200 km from the Ebro LMA, then terminated near the centroid of the network. Is that correct? There can be substantial changes in both source detection efficiency and solution accuracy over that distance, which could impact the timing of the features noted, but those limitations are not discussed in the interpretation of the results.

Agreed. In this regard, we have analyzed the LMA network sensitivity during the present case study. An appendix has been added in this regard. The added figure shows a lack of sensitivity during the first period of development. We have included this data in the results description.

The flash grouping (and therefore counting and jump identification): While this is a small part of the overall discussion, it is significantly different from what's been presented in prior literature and needs further discussion. Many papers use a minimum of 10 VHF sources per flash, including the Schultz et al. (2009, 2017), and Chronis et al. (2015) studies, all of which used LMA data, and none of which are mentioned in section 4g. Given the dominance of small flash sizes near convective cores (Bruning and MacGorman 2013), it could be expected that a minimum of 50 VHF sources will miss many of the flashes which might have otherwise contributed to the assignment of a lightning jump. [And this is independent of the network sensitivity which has led to some studies using even fewer sources per flash (Fuchs et al. 2015).] The presented rates appear very low compared to what I would expect based on the plots presented. Without demonstration of the sensitivity to the number of sources, these results cannot be contrasted to prior literature.

After reviewing data processing to apply the 10-source filter instead of the 50-source, we realized LMA data was unfiltered. We applied, therefore, the 10-source filter in the lightning clustering algorithm. After this, the lightning-jump technique (Gatlin and Goodman, 2010) has been used to retrieve the lightning jumps. Text in the manuscript has been changed accordingly.

Radar intercomparison: The authors could better present the case for using lightning features with a little more focus on the radar intercomparison. For example, the heights of the BWER slices shown in *[original figure numbers]* Fig. 8 could be presented for more direct comparison with Fig. 7. And the LMA sources overlaid on the cross sections of Figs. 9 and 12 (note: Fig. 12 was not referenced in text) for more direct comparison. Like Chmielewski et al. 2020 and others, the authors may discover some interesting offsets due to particle motions.

Thanks for the suggestion. Sparkles detected by the LMA have been overlaid to the radar cross sections (now Fig. 11). We have ensured that all figures are referenced in the text.

Overshooting-top signature: The overshooting-top signature, or "sparkles," could be demonstrated to the reader in a much more convincing manner than the single snapshot(s). The authors could follow the examples of Emersic et al. (2011) and/or MacGorman et al. (2017) to show the complete time evolution instead of describing the evolution and asking for the reader to trust them. Relatedly, MacGroman et al. (2017) found that the overshooting top signature, or "sparkles," were relatively bounded by the 18-dB*Z* and 30-dB*Z* echo tops. While the authors suggest analyzing similar levels (15 and 35 dBZ), only the 15- and 50-dB*Z* levels are shown (Fig.14). The authors could both better demonstrate their evolution and show the echo tops on the same plot to support their intercomparison.

A new figure (Fig. 7) has been added to show the complete time vs. height evolution of the LMA sources. As commented, we have changed the approach of the results presented by analyzing the evolution of the storm instead of focusing only on severe weather signatures. The new section better relates the different observation systems, like the relation between radar and sparkles.

[Fig. 14] could have been much more useful for bringing together the myriad of features discussed. Better aligning the different components would support the authors claims that the lightning signals are useful early warning indicators and/or storm intensity signals. For example:

- Multiple periods of sparkles were noted in text, but only one time period marked here.
- The periods with discussed satellite features are not marked.
- The period with the three-body scatter spike is not marked.
- The period with a BWER is not marked.
- The time of cell splitting is not marked.
- The time periods with ERA5 analysis could have been marked.
- A subset of the average freezing heights from Table 2 could have been highlighted.
- The flash rates appear to be plotted every 10 minutes but are 1-minute rates? One of the benefits of lightning is the continuous nature of the dataset, which could be highlighted by plotting at 1-minute intervals.

Thanks for the suggestion. We have modified this figure (now Figure 6 in the main text) following reviewer's recommendations. The first subplot shows LMA source density and intra-cloud flash rate (1-min data, min^{-1}). Lightning jumps are also indicated, and the period during which LMA data are not reliable due to the storm location relative to the LMA network is shaded in grey. The second subplot presents echo-top heights (TOP-15, TOP-35, and TOP-50, in km ASL), maximum reflectivity (dBZ), and vertically integrated liquid (VIL, mm). In addition, the altitudes of the 0°C, −10°C, −20°C, and −40°C isotherms, as well as the equilibrium level retrieved from ERA5 (at 13 UTC), are shown. The third subplot depicts observed severe-weather signatures (sparkles, lightning hole—LH, storm splitting, bounded weak-echo region—BWER, three-body scatter spike—TBSS, V-shaped cloud top, overshooting top, and above-anvil cirrus plume—AACP). Finally, the fourth subplot shows the severe-weather reports (hail, downbursts, and tornado).

References mentioned:

Bruning, E. C., and D. R. MacGorman, 2013: Theory and observations of controls on lightning flash size spectra. *J. Atmos. Sci.*, **70**, 4012–4029.
Chmielewski, V. C., D. R. MacGorman, C. L. Ziegler, E. DiGangi, E., D. Betten, and M. Biggerstaff, M., 2020: Microphysical and transportive contributions to normal and anomalous polarity subregions in the 29–30 May 2012 Kingfisher storm. *J. Geophys. Res. Atmos.*, **125**, e2020JD032384.
Fuchs, B. R., S. A. Rutledge, E. C. Bruning, J. R. Pierce, J. K. Kodros, T. J. Lang, D. R. MacGorman, P. R. Krehbiel, and W. Rison. 2015: Environmental controls on storm intensity and charge structure in multiple regions of the continental United States. *J. Geophys. Res. Atmos.*, **120**, 6575–6596.
Schultz, C. J., W. A. Petersen, and L. D. Carey, 2009: Preliminary development and evaluation of lightning jump algorithms for the real-time detection of severe weather. *J. Appl. Meteor. Climatol.*, **48**, 2543–2563.
——, L. D. Carey, E. V. Schultz, and R. J. Blakeslee, 2017: Kinematic and microphysical significance of lightning jumps versus nonjump increases in total flash rate. *Wea. Forecasting*, **32**, 275–288.

Thank you for the complementary references.

[Minor comments omitted…]

Second Review:

Recommendation: Accept with minor revisions.

Overall Comments: I thank and applaud the authors for the modifications they have made to this manuscript. It is much easier in the current revision to interpret how the different features fit together and might be used to describe total storm state in future cases. The presented analysis, with the adjusted LMA flash clustering, filtering, and jump identification, is now much easier to compare to prior research and theoretical expectations. I believe this case study will be an important and useful component of the lightning paradigm.

All of my remaining comments are minor suggestions.

[Minor comments omitted…]

REVIEWER B (Cameron J. Nixon):

Initial Review:

Recommendation: Accept with minor revisions.

Summary: This paper clearly and convincingly achieves its goal of advocating for the use of lightning data in the severe-weather warning process. I especially appreciate the authors' way of showing a real-life severe-storm through multiple observational products/perspectives. I consider it acceptable with minimal edits, most of which are small/grammatical.

We greatly appreciate your review. In light of the comments (mostly from the other reviewer), the study has undergone major changes, including section rearrangements, figure addition, reference addition, and many other minor changes. We have addressed most of your suggestions, as noted below.

[Editor's Note: A few of the "minor comments" seemed substantive enough to include in the review revcord, and are reproduced below.]

Substantive Comments: Since you're doing this study on hail and lightning, the freezing level is also critical!

Yes, we retrieved several significant temperature levels (0, –10, –20, –40°C) for our analysis. According to another comment from your review, we have specified here all the levels analyzed.

A seemingly significant finding in the abstract was that a "jump" in sparkles preceded the jump in ICF rate, and thereby offered more lead time. The authors should speak more on this here, and compare the exact times which both jumps started and ended, relative to the production of both hail and the tornado.

Following this suggestion, this section has been rewritten and enlarged.

Given that some thermodynamic environments and storm evolutions are less conducive to lightning than others, and some supercells fail to produce as much lightning as others, would this change any of your recommendations to forecasters? Could you speak on when these features may not be detectable?

The conclusions section has been rewritten.

[Minor comments omitted…]

Second Review:

Recommendation: Accept.

[No accompanying comments...]